RESEARCH ARTICLE

The mechanism of MICU-dependent gating of the mitochondrial Ca^{2+}uniporter

Vivek Garg[1,2]*, Junji Suzuki[1], Ishan Paranjpe[1], Tiffany Unsulangi[1], Liron Boyman[2], Lorin S Milescu[3], W Jonathan Lederer[2], Yuriy Kirichok[1]*

[1]Department of Physiology, University of California San Francisco, San Francisco, United States; [2]Department of Physiology, University of Maryland, Baltimore, United States; [3]Department of Biology, University of Maryland, College Park, United States

Abstract Ca^{2+} entry into mitochondria is through the mitochondrial calcium uniporter complex (MCU_{cx}), a Ca^{2+}-selective channel composed of five subunit types. Two MCU_{cx} subunits (MCU and EMRE) span the inner mitochondrial membrane, while three Ca^{2+}-regulatory subunits (MICU1, MICU2, and MICU3) reside in the intermembrane space. Here, we provide rigorous analysis of Ca^{2+} and Na^{+} fluxes via MCU_{cx} in intact isolated mitochondria to understand the function of MICU subunits. We also perform direct patch clamp recordings of macroscopic and single MCU_{cx} currents to gain further mechanistic insights. This comprehensive analysis shows that the MCU_{cx} pore, composed of the EMRE and MCU subunits, is not occluded nor plugged by MICUs during the absence or presence of extramitochondrial Ca^{2+} as has been widely reported. Instead, MICUs potentiate activity of MCU_{cx} as extramitochondrial Ca^{2+} is elevated. MICUs achieve this by modifying the gating properties of MCU_{cx} allowing it to spend more time in the open state.

***For correspondence:**
vgarg@som.umaryland.edu (VG);
yuriy.kirichok@ucsf.edu (YK)

Competing interests: The authors declare that no competing interests exist.

Funding: See page 24

Preprinted: 05 April 2020
Received: 11 April 2021
Accepted: 09 August 2021
Published: 31 August 2021

Reviewing editor: Richard S Lewis, Stanford University School of Medicine, United States

Introduction

Mitochondrial Ca^{2+} uptake regulates ATP production by modulating the activities of several dehydrogenases in the mitochondrial matrix primarily the pyruvate dehydrogenase and likely other control systems (***Glancy and Balaban, 2012***; ***McCormack et al., 1990***; ***McCormack and Denton, 1993***; ***Wescott et al., 2019***). Matrix Ca^{2+} ($[Ca^{2+}]_m$) also plays a crucial role in influencing cell fate (***Bernardi, 1999***; ***Berridge et al., 2003***; ***Glancy and Balaban, 2012***; ***Gunter et al., 2010***). Physiological and pathological Ca^{2+} signaling in mitochondria depend on Ca^{2+} entry into the matrix (***Holmström et al., 2015***; ***Kwong et al., 2015***; ***Luongo et al., 2017***) and its extrusion through the mitochondrial sodium-calcium exchanger (***Boyman et al., 2013***; ***Luongo et al., 2015***; ***Palty et al., 2010***) and other mechanisms (***Bernardi, 1999***; ***Gunter et al., 2010***). Ca^{2+} entry is mediated by the mitochondrial Ca^{2+} uniporter holocomplex (MCU_{cx}) (***Bernardi, 1999***; ***Deluca and Engstrom, 1961***; ***Gunter et al., 2010***), a Ca^{2+}-selective channel that is regulated by the intracellular (extra-mitochondrial) $[Ca^{2+}]$ level ($[Ca^{2+}]_i$) (***Fieni et al., 2012***; ***Kirichok et al., 2004***). The MCU_{cx} is composed of five distinct subunits types, two of which span the inner mitochondrial membrane (IMM) - MCU and EMRE - and two of the three MICU subunits (MICU1, MICU2, and MICU3) which reside in the intermembrane space (***Baughman et al., 2011***; ***De Stefani et al., 2011***; ***Sancak et al., 2013***). MICU1 connects an EMRE subunit in the MCU_{cx} with a second MICU subunit. Recent structural discoveries (***Wang et al., 2019***; ***Fan et al., 2020***; ***Wang et al., 2020b***; ***Zhuo et al., 2021***) suggest that the functioning channel is a dimer composed of two MCU/EMRE pores joined through the N-terminal of MCU subunits in the matrix, and MICU subunits in the intermembrane space.

For Ca^{2+} to enter the matrix, Ca^{2+} must first permeate the outer mitochondrial membrane (OMM) through the largely open VDAC (voltage-dependent 'anion' channel), a beta-barrel channel into the intermembrane space (IMS). From the IMS, Ca^{2+} crosses the nearly impermeant inner

mitochondrial membrane (IMM) in a highly regulated manner into the mitochondrial matrix through the small conductance, highly selective MCU_{cx} (**Kirichok et al., 2004**; **Williams et al., 2013**). The recent dynamic and exciting body of work investigating Ca^{2+} movement through the MCU_{cx} has led to a number of controversial and perplexing reports (**Csordás et al., 2013**; **Tomar et al., 2019**; **Foskett and Madesh, 2014**; **Gottschalk et al., 2019**; **Hoffman et al., 2013**; **Mallilankaraman et al., 2012b**; **Nemani et al., 2018**; **Perocchi et al., 2010**; **Tufi et al., 2019**; **Supplementary file 1a and b**). These publications also provoke the possibility that the molecular components of MCU_{cx} have additional broad actions in mitochondria which could complicate our understanding (**Tomar et al., 2019**; **Gottschalk et al., 2019**; **Tufi et al., 2019**). Here, we use an array of quantitative tools to directly examine the conductance of the MCU_{cx} channel and how it is gated by MICU subunits. Our investigation provides reasons to question some of the published working hypotheses and suggest a new view of the molecular gating of MCU_{cx}.

Results

Quantitative assessment of the MCU_{cx} and its subunits

A whole mitoplast patch clamp method was used to measure whole IMM current to assess MCU_{cx} function (**Fieni et al., 2012**; **Garg and Kirichok, 2019**; **Kirichok et al., 2004**) and determine how the subunits contribute to the measured MCU_{cx} current. Mitochondria were isolated from DRP1 knockout (KO) mouse embryonic fibroblasts (MEFs) (**Ishihara et al., 2009**). DRP1 is encoded by the *Dnm1l*. The DRP1-KO MEFs were used to prepare mitoplasts using a French Press. This cell line was chosen as the source for many experiments because it provided a significantly higher proportion of large isolated mitoplasts and enabled the recording of stable MCU_{cx} currents with a favorable signal-to-noise ratio. We confirmed that this cell line expresses all principal subunits of the MCU complex (**Figure 1—figure supplement 1**). Importantly, the MCU_{cx} was intact in isolated mitoplasts, and its composition was the same as in intact mitochondria (**Figure 1—figure supplement 2F**). We also generated gene knockouts for all principal subunits of the MCU complex (MCU, EMRE, and MICU1−3) using CRISPR-Cas9 in this cell line (**Figure 1—figure supplement 1**). MCU, EMRE, and MICU1−3 are encoded by the *Mcu*, *Smdt1* and *Micu1−3* genes, respectively.

Figure 1A shows the $[Ca^{2+}]_i$ dependence of the MCU_{cx} current in mitoplasts from WT DRP1-KO MEFs, and shows the absence of Ca^{2+} current (I_{Ca}) in MCU-KO or EMRE-KO. Additionally, it shows an important feature of the MCU_{cx}; in the absence of extramitochondrial Ca^{2+} (control trace), there is outward current at positive potentials resulting from the efflux of Na^+ through the MCU_{cx} due to the 110 mM Na^+ gluconate in the matrix from the patch pipette (**Figure 1A**, **Figure 1—figure supplement 2D and E**). When extramitochondrial Ca^{2+} is present, Ca^{2+} enters the selectivity filter of the MCU_{cx} channel to block Na^+ permeation (**Fieni et al., 2012**; **Garg and Kirichok, 2019**; **Kirichok et al., 2004**) and no outward current is seen. Importantly, MCU_{cx} currents can be rescued by the ectopic expression of the MCU and EMRE subunits in their corresponding knockout cell lines (**Figure 1B and C**, **Figure 1—figure supplement 2G and H**). From these results, the DRP1-KO MEFs recapitulate key findings in previous publications (**Chaudhuri et al., 2013**; **Fieni et al., 2012**; **Kirichok et al., 2004**; **Sancak et al., 2013**). We show an additional novel observation, important to our later experiments, that when Na^+ is used to replace Ca^{2+} in the cytosolic compartment (i.e. the bath solution), an MCU-mediated Na^+ current (I_{Na}) is observed, and this current also depends on the presence of MCU and EMRE (**Figure 1D and E**, **Figure 1—figure supplement 2D and E**).

In intact WT cells, the $[Ca^{2+}]_i$ increase (elicited by SERCA inhibitor thapsigargin) was followed, after a short delay, by $[Ca^{2+}]_m$ elevation as detected by a genetically-encoded Ca^{2+} indicator *Cepia* targeted to mitochondria (**Suzuki et al., 2014**; **Figure 1—figure supplement 2A**). However, as expected, in MCU-KO or EMRE-KO cell lines that have no functional MCU_{cx} (**Baughman et al., 2011**; **De Stefani et al., 2011**; **Sancak et al., 2013**), no significant $[Ca^{2+}]_m$ elevation was observed (**Figure 1—figure supplement 2B and C**).

One of the controversial elements in previously published experiments is the explanation of the cause of the 'threshold' of the MCU_{cx} Ca^{2+} influx into the matrix (**Csordás et al., 2013**; **Tomar et al., 2019**; **Foskett and Madesh, 2014**; **Hoffman et al., 2013**; **Mallilankaraman et al., 2012b**; **Perocchi et al., 2010**; **Tufi et al., 2019**). It was noted initially (**Mallilankaraman et al., 2012b**) that there is a cytosolic concentration of Ca^{2+} ($[Ca^{2+}]_i$) below which there is no MCU_{cx}-

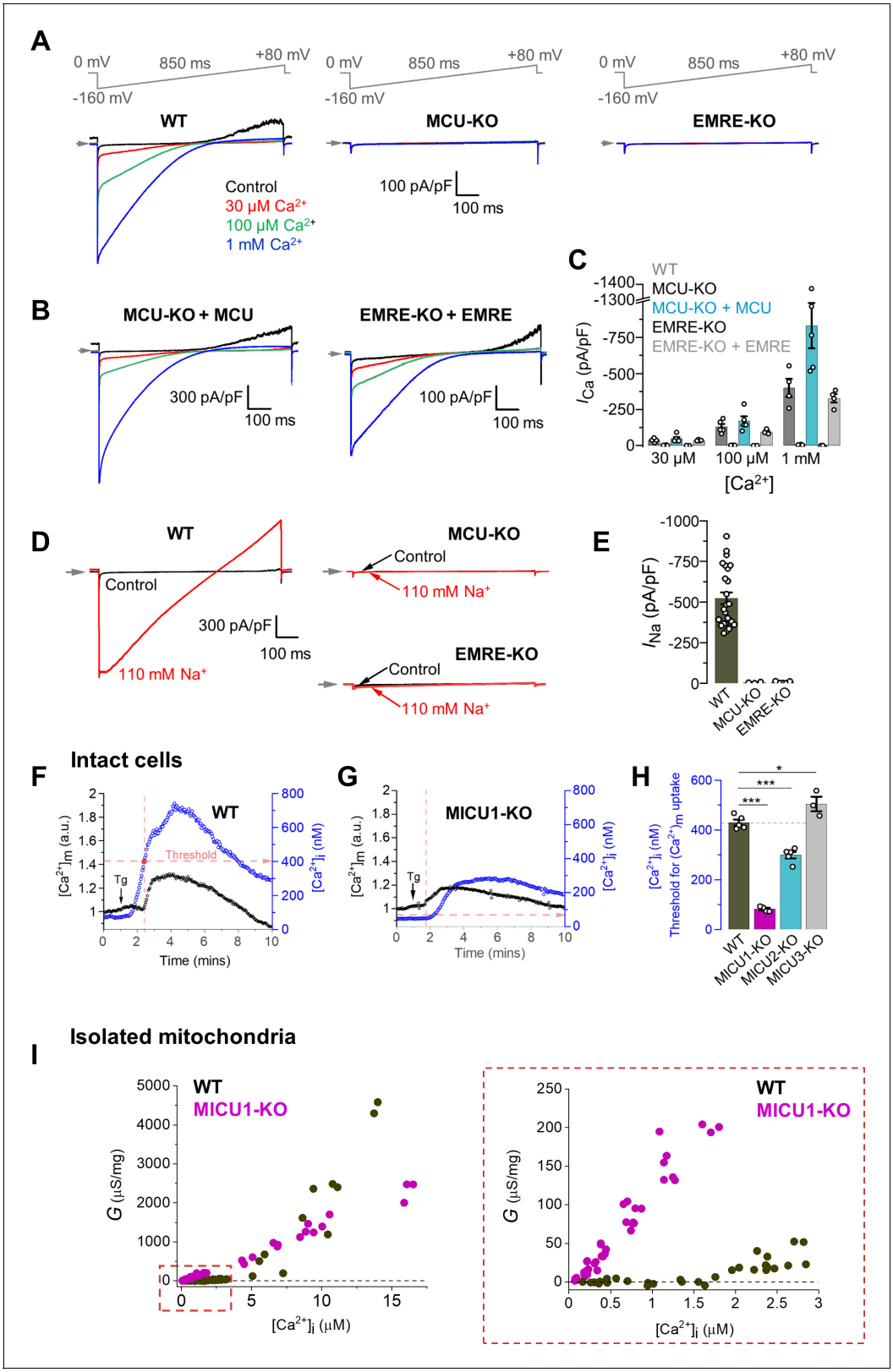

Figure 1. Characterization of MCU_{cx} properties in isolated mitoplasts, intact cells, and isolated mitochondria from MEFs. (**A**) Inward I_{Ca} elicited by a voltage ramp in WT, MCU-KO and EMRE-KO mitoplasts exposed to $[Ca^{2+}]_i$ of 30 μM, 100 μM, and 1 mM. In WT, also note an outward Na^+ current via MCU at positive voltages in Ca^{2+}-free bath solution (Control). Voltage protocol is indicated on the top. All superimposed current traces in a single panel are from the same mitoplast. (**B**) I_{Ca} is rescued by the recombinant expression of MCU and EMRE in their respective knockout cell lines. (**C**) I_{Ca}

Figure 1 continued on next page

Figure 1 continued

density measured at −160 mV at different $[Ca^{2+}]_i$ in indicated cell lines; n = 4–5. (**D**) Representative I_{Na} in WT, MCU-KO and EMRE-KO mitoplasts at 110 mM $[Na^+]_i$. (**E**) I_{Na} density measured at −80 mV in WT, MCU-KO, and EMRE-KO mitoplasts; n = 3–20. (**F and G**) Representative $[Ca^{2+}]_m$ (*black*, left ordinate) and $[Ca^{2+}]_i$ (*blue*, right ordinate) in an individual cell with (**F**) WT MCU_{cx}, and (**G**) MICU1 knockout before and after application of 300 nM thapsigargin (Tg, arrow). Dashed red lines indicate the $[Ca^{2+}]_i$ at which the $[Ca^{2+}]_m$ starts to increase ('Threshold'). (**H**) $[Ca^{2+}]_i$ threshold for $[Ca^{2+}]_m$ elevation in WT and indicated knockout cell lines; n = 3–4 dishes, total cells = ~150 each group. Data shown as mean ± SEM; one-way ANOVA with post-hoc Tukey test. Statistics was run on number of dishes. (**I**) Ca^{2+} conductance (G) of the IMM plotted as a function of $[Ca^{2+}]_i$. Right panel shows the zoomed-in region for $[Ca^{2+}]_i$ between 0 and 3 μM; n = 64–75 independent experiments, N = 4–7 independent preparations, all data is shown. All superimposed current traces in a single panel are from the same mitoplast. Data shown as mean ± SEM.
The online version of this article includes the following source data and figure supplement(s) for figure 1:

Source data 1. Dataset values for ***Figure 1***.
Figure supplement 1. Generation of knockouts for various MCU_{cx} subunits.
Figure supplement 1—source data 1. Raw western blot image for panel G.
Figure supplement 1—source data 2. Raw western blot image for panel H.
Figure supplement 1—source data 3. Raw western blot image for panel I.
Figure supplement 1—source data 4. Real time PCR (Ct) values for different genes.
Figure supplement 2. $[Ca^{2+}]_m$ phenotype in cells deficient for various MCU_{cx} subunits, patch clamp methodology, and protein expression of various MCU_{cx} subunits in isolated mitoplasts and MEFs.
Figure supplement 2—source data 1. Raw western blot image for panel F.
Figure supplement 2—source data 2. Raw western blot image for panel G.
Figure supplement 2—source data 3. Raw western blot image for panel H.
Figure supplement 3. Mitochondrial Ca^{2+} uptake phenotype in cells and mitochondria deficient for MICU subunits.
Figure supplement 3—source data 1. Dataset values for ***Figure 1—figure supplement 3***.

medicated Ca^{2+} influx. ***Figure 1F*** shows that such a threshold for DRP1-KO WT MEF is indeed found at around 400 nM Ca^{2+}. This threshold is largely gone in MICU1-KO cells (***Figure 1G***). In MICU2-KO and MICU3-KO cells, the changes in the threshold levels are shown in ***Figure 1H***, and ***Figure 1—figure supplement 3A–D***. Past studies of other investigators have used similar information from their MICU1-KO cells to argue that MICU1 forms a 'plug' or an occlusion in the channel pore. This implies that in MICU1-KO cells, the MCU_{cx} conductance should be greater due to the removal of the plug. This conclusion, however, is challenged by the Ca^{2+} conductance studies shown here in isolated mitochondria from WT MEFs shown in ***Figure 1I*** and ***Figure 1—figure supplement 3E***. While the Figure shows increased conductance of MCU_{cx} at low $[Ca^{2+}]_i$ in the MICU1-KO mitochondria consistent with the removal of a putative MCU_{cx}'plug', there is decreased conductance at high $[Ca^{2+}]_i$ (~8 μM or higher), an observation that is inconsistent with the plug hypothesis (***Mallilankaraman et al., 2012b***). Additional recent modifications of this hypothesis add the prediction that allosteric actions of MICU1 on MCU_{cx} account for any inconsistencies or contradictions of the plug hypothesis (***Csordás et al., 2013***). Moreover, new findings suggest that there may be broad actions of MICU1 on non-MCU_{cx} targets within the mitochondria (***Tomar et al., 2019***; ***Gottschalk et al., 2019***; ***Tufi et al., 2019***). These findings and the unrefined and untested modifications of the plug hypothesis motivate additional investigations. We have carried out new quantitative experiments and analysis that may help us better understand how MICU1 works in the context of the MCU_{cx} as is shown in ***Figure 2***.

MICUs are $[Ca^{2+}]_i$-dependent MCU_{cx} potentiators

To investigate how MICU1 works, I_{Ca} was measured in mitoplasts at five extramitochondrial $[Ca^{2+}]_i$ levels, 10 μM, 100 μM, 1 mM, 5 mM, and 25 mM (***Figure 2A and B***, and ***Figure 2—figure supplement 1A–C***). WT mitoplasts show I_{Ca} records similar to the current density measurements from MICU2-KO and MICU3-KO mitoplasts. In contrast, WT mitoplasts have I_{Ca} current densities that are roughly twice the size of the current densities from the MICU1-KO mitoplasts. This finding is like the conductance measurements at elevated $[Ca^{2+}]_i$ in ***Figure 1I*** and thus inconsistent with the plug hypothesis that posits that MICU1 is an obstructing plug of MCU_{cx}.

The expression of EMRE protein (but not MCU) was significantly reduced in MICU1-KO (***Figure 2—figure supplement 1D–F***), as was also shown previously (***Liu et al., 2016***). However, the lower EMRE expression in MICU1-KO was not a limiting factor for I_{Ca}, because EMRE overexpression

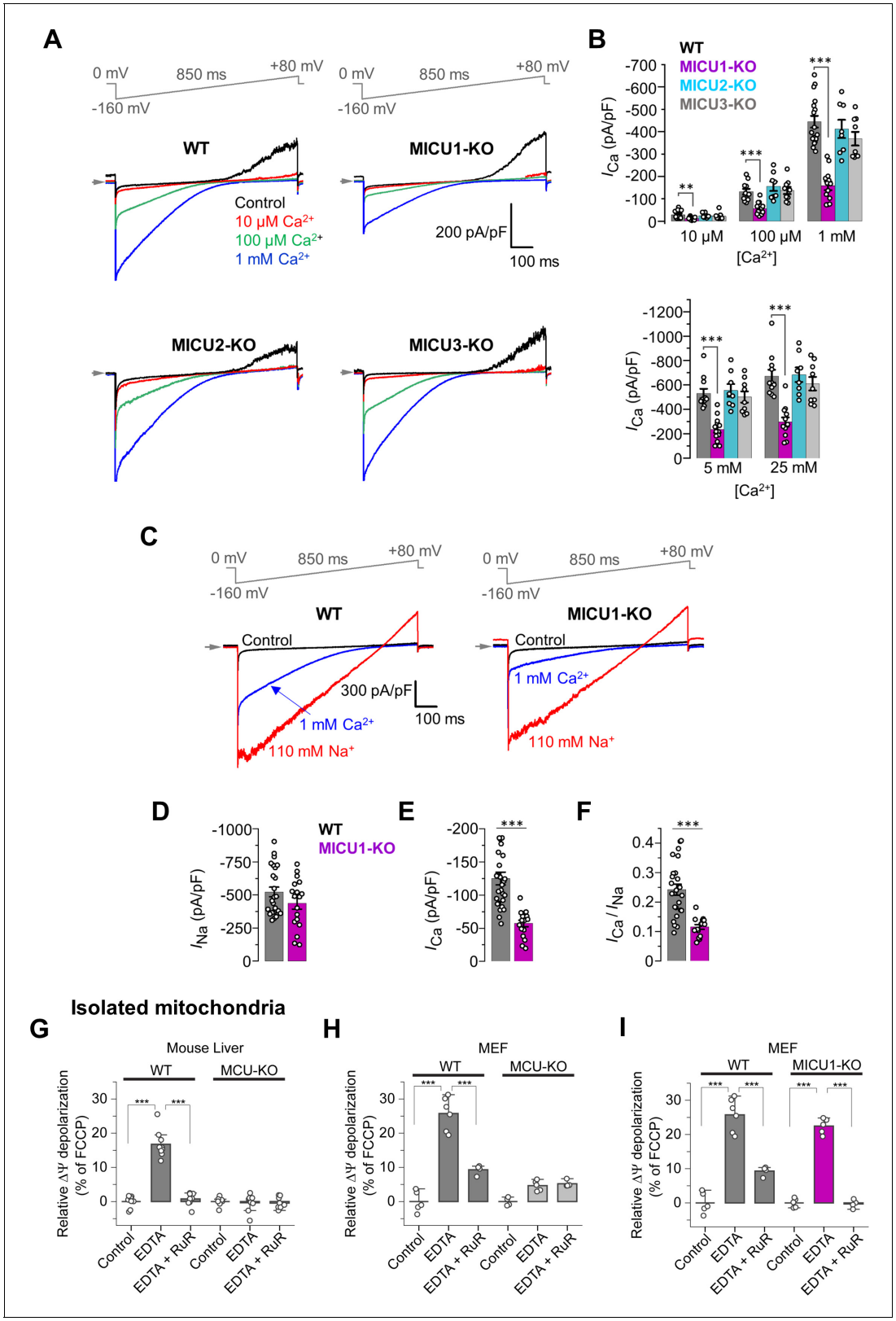

Figure 2. MICUs are $[Ca^{2+}]_i$-dependent MCU_{cx} potentiators. (**A**) Inward I_{Ca} in WT, MICU1-KO, MICU2-KO, and MICU3-KO mitoplasts exposed to 10 µM, 100 µM and 1 mM $[Ca^{2+}]_i$. (**B**) I_{Ca} densities measured at −160 mV and $[Ca^{2+}]_i$ of 10 µM, 100 µM, and 1 mM (*upper*), as well as 5 mM and 25 mM (*lower*). Data shown as mean ± SEM; one-way ANOVA with post-hoc Tukey test, n = 8–17. (**C**) Representative I_{Ca} (*blue*) and I_{Na} (*red*) recorded from the same WT and MICU1-KO mitoplasts exposed to 1 mM $[Ca^{2+}]_i$ or 110 mM $[Na^+]_i$ in the absence of Ca^{2+}. (**D–F**) Amplitudes of I_{Na} (**D**) and I_{Ca} (**E**), as well

Figure 2 continued on next page

Figure 2 continued

as the I_{Ca}/I_{Na} ratio (**F**) in the same WT and MICU1-KO mitoplasts. Currents were measured at −80 mV. Data shown as mean ± SEM; unpaired t-test, two-tailed, n = 18–27. (**G and H**) ΔΨ depolarization induced by application of 5 mM EDTA in suspension of isolated mitochondria from mouse liver (**G**) and MEF (**H**). The degree of depolarization is expressed as percentage of the full depolarization induced by 1 μM FCCP. Both WT and MCU-KO mitochondria were assessed. Data shown as mean ± SEM; one-way ANOVA with Tukey test, n = 4–9. (**I**) ΔΨ depolarization induced by application of 5 mM EDTA in suspension of isolated mitochondria from MEF with WT and MICU1-deficient MCU_{cx}. WT data in panel I is the same as in panel H. The degree of depolarization is expressed as percentage of the full depolarization induced by 1 μM FCCP. Data shown as mean ± SEM; one-way ANOVA with Tukey test, n = 4–5. All superimposed current traces in a single panel are from the same mitoplast.

The online version of this article includes the following source data and figure supplement(s) for figure 2:

Source data 1. Dataset values for ***Figure 2***.
Figure supplement 1. I_{Ca} in MICU1–3 knockouts, and expression levels of various MCU subunits in MICU1-KO.
Figure supplement 1—source data 1. Raw western blot image for panel D.
Figure supplement 1—source data 2. Raw western blot image for panel E.
Figure supplement 1—source data 3. Raw western blot image for panel F.
Figure supplement 1—source data 4. Raw western blot image for panel G.
Figure supplement 1—source data 5. Dataset values for ***Figure 2—figure supplement 1***.
Figure supplement 2. The sensitivity of I_{Na} to $[Ca^{2+}]_i$ remains unchanged in MICU1-KO.
Figure supplement 2—source data 1. Dataset values for ***Figure 2—figure supplement 2***.
Figure supplement 3. DRP1 does not affect the currents mediated by the MCU_{cx} or their phenotype in MICU1-KO.
Figure supplement 3—source data 1. Dataset values for ***Figure 2—figure supplement 3***.

in MICU1-KO cells did not rescue the I_{Ca} reduction (***Figure 2—figure supplement 1G–I***). Therefore, the I_{Ca} reduction in MICU1-KO was not caused by reduction in MCU or EMRE.

To better understand the role played by the MICU1 subunit in the function of the MCU_{cx}, we used a novel test to characterize the MCU_{cx} channel properties independent of Ca^{2+} conductance. We used Na^+ current via MCU_{cx} (I_{Na}) in the absence of both Ca^{2+} and Mg^{2+} (using EDTA) (***Fieni et al., 2012***; ***Garg and Kirichok, 2019***; ***Kirichok et al., 2004***), to calibrate I_{Ca} and characterize MCU_{cx} as shown in ***Figure 2C–D***. Here, it is shown that the Na^+ current through MCU_{cx} is indistinguishable in magnitude when it is measured in WT and MICU1-KO mitoplasts (***Figure 2D***). This provides evidence that the MCU_{cx} conductance pathway is the same in WT and MICU1-KO. Nevertheless, when Ca^{2+} permeates MCU_{cx}, the I_{Ca} in WT is roughly twice that of the current through MICU1-KO mitoplasts (***Figure 2E***). Also, the I_{Ca}/I_{Na} ratio as measured in the same mitoplast decreased approximately twice in MICU1-KO in comparison to WT (***Figure 2F***). Importantly, the reduction in I_{Ca}/I_{Na} ratio in MICU1-KO could not be explained by altered relative affinities for Ca^{2+} and Na^+ binding in the selectivity filter, because I_{Na} was inhibited to the same extent by 2 nM $[Ca^{2+}]_i$ in both WT and MICU1-KO mitoplasts (***Figure 2—figure supplement 2A and B***). From this we conclude that the MICU1 subunit enhances the MCU current at high $[Ca^{2+}]_i$ and does not occlude the MCU_{cx} channel when $[Ca^{2+}]_i$ is low.

We also reproduced these results in MEFs with intact DRP1 (*Dnm1l*$^{+/+}$). In these cells, the amplitudes of I_{Ca} and I_{Na} were the same as in *Dnm1l*$^{-/-}$ MEFs (***Figure 2—figure supplement 3A and B***). Similar to MICU1 knockout in *Dnm1l*$^{-/-}$ MEFs, MICU1 knockout in *Dnm1l*$^{+/+}$ MEFs did not affect I_{Na} while markedly reduced I_{Ca} (***Figure 2—figure supplement 3C–E***). Additionally, MICU1-KO reduced the I_{Ca}/I_{Na} ratio, as measured in the same mitoplast, to the similar extent in *Dnm1l*$^{+/+}$ MEFs (***Figure 2—figure supplement 3F***). Thus, as expected, Drp1 presence or absence does not affect currents mediated by the MCU complex or the MICU1-KO phenotypes.

The lack of the MCU_{cx} occlusion by MICU1 at low $[Ca^{2+}]_i$ was further tested in intact isolated mitochondria as shown in ***Figure 2G–I***. In these experiments, we found that depletion of Ca^{2+} and Mg^{2+} using EDTA enables a Na^+ influx via MCU_{cx} that depolarizes $\Delta\Psi_m$ (***Figure 2G and H***). As shown in ***Figure 2I***, this influx depolarizes $\Delta\Psi_m$ to the same extent whether MICU1 was expressed or not, again showing the lack of MCU_{cx} occlusion by MICUs.

Since in MICU1-KO, all MICUs are removed from the MCU_{cx} complex, we conclude that MICUs do not plug the MCU_{cx} channel when $[Ca^{2+}]_i$ is low. Instead, the function of MICUs is to potentiate MCU_{cx} activity at elevated $[Ca^{2+}]_i$.

Role of the Ca^{2+}-binding EF hands of MICUs

The Ca^{2+}-dependent potentiation of MCU_{cx} imparted by the MICU subunits is likely to be mediated by Ca^{2+} binding to their EF hands. To test this hypothesis, we recombinantly expressed MICU1–3 or MICU1–3 with mutated EF hands (mut-EF-MICU, to disable Ca^{2+} binding ***Kamer et al., 2017***) in their respective knockout cell lines [***Figure 3A***] and examined the changes in I_{Ca}. Expression levels of both the recombinant WT and mut-EF-MICU proteins were significantly higher as compared to endogenous MICUs expression in each case (***Figure 3A***).

In MICU1-KO, expression of MICU1 was able to restore I_{Ca} to the WT level, but mut-EF-MICU1 expression failed to do so (***Figure 3B***). This confirms our hypothesis that Ca^{2+} binding to the EF hands of MICU1 is indispensable for the I_{Ca} potentiation.

In MICU2-KO, I_{Ca} was not significantly affected (***Figure 3C***, and ***Figure 2A and B***), because the loss of MICU2 appeared to be compensated with increased MICU1 expression and formation of MICU1 homodimers (***Patron et al., 2014***; ***Figure 3—figure supplement 1A***). Therefore, overexpression of recombinant MICU2 in the knockout background only reverted the MICU1 homodimer back to heterodimer without any change in the I_{Ca} amplitude (***Figure 3C***). In contrast, mut-EF-MICU2 overexpression displaced MICU1 from the homodimers in favor of MICU1/mut-EF-MICU2 heterodimer, leading to a decrease in the total number of functional EF hands in the heterodimer. This results in a significant decrease in MICU-dependent I_{Ca} potentiation (***Figure 3C***). These functional data, combined with biochemical/structural evidence for preferential formation of MICU1/MICU2 heterodimers (***Fan et al., 2020***; ***Patron et al., 2014***; ***Petrungaro et al., 2015***; ***Wang et al., 2019***; ***Wang et al., 2020a***; ***Wang et al., 2020b***; ***Xing et al., 2019***; ***Zhuo et al., 2021***), suggest that MICU2, along with MICU1, is responsible for allosteric potentiation of MCU upon binding of cytosolic Ca^{2+} to their EF hands.

The composition of MICU dimers can also be affected by MICU3 that, similar to MICU2, was proposed to interact and form heterodimers with MICU1 (***Patron et al., 2019***; ***Plovanich et al., 2013***). MICU3 is a minor protein as compared to MICU1 and 2 in the majority of tissues and cell lines (***Patron et al., 2019***), which also appears to be the case in our system (***Figure 3A***). Accordingly, I_{Ca} was not affected in MICU3-KO mitoplasts, and overexpression of recombinant MICU3 or mut-EF-MICU3 in MICU3-KO also had no effect on I_{Ca} (***Figure 3D***). MICU3 is profoundly expressed in neurons where it was shown to increase the efficiency of mitochondrial Ca^{2+} uptake in axons (***Ashrafi et al., 2020***).

Ca^{2+} binding to the EF hands of MICU subunits and a subsequent conformational change that potentiates the MCU_{cx} activity require a finite time and may delay I_{Ca} activation/deactivation in response to rapid changes in $[Ca^{2+}]_i$. Therefore, we examined I_{Ca} activation and deactivation kinetics in response to rapid changes in $[Ca^{2+}]_i$ and tested whether they depend on MICUs. I_{Ca} activation upon rapid elevation of $[Ca^{2+}]_i$ from virtually Ca^{2+}-free to 1 mM was immediate, with kinetics comparable to the rate of solution exchange (τ ~0.4 ms) achieved by our fast application system (***Figure 3E***, and ***Figure 3—figure supplement 2***). Importantly, the kinetics of the I_{Ca} rapid response was not altered in MICU1-KO (***Figure 3E and F***). The deactivation kinetics was similarly fast and not dependent on MICU1 (***Figure 3E and F***). The result of these experiments correspond to the previous observation that EF hands of calmodulin bind Ca^{2+} with a µs time constant (***Faas et al., 2011***). The conclusion from these experiments is that the kinetics of Ca^{2+} binding to the MICU's EF hands, and the resultant conformational change in the MCU_{cx}, are fast enough that MICUs and mitochondria will rapidly track changes in $[Ca^{2+}]_i$.

The MCU_{cx} is an inward rectifying Ca^{2+} channel (***Kirichok et al., 2004***). However, it remains unclear if the MICUs contribute to this feature. To examine this possibility, we measured I_{Ca} in the presence of 2 mM $[Ca^{2+}]_m$ (pipette solution). Under these conditions, no outward I_{Ca} was observed either before or after $[Ca^{2+}]_i$ elevation in either WT or MICU1-KO. However, as expected, 1 mM $[Ca^{2+}]_i$ induced a robust inward I_{Ca} (***Figure 3G***). Thus, the MICUs do not appear to be responsible for the inward rectification of MCU_{cx}, and the inward rectification is an inherent property of the pore proteins.

Recently published work suggested that MCU_{cx} might be inhibited by matrix $[Ca^{2+}]$ (***Vais et al., 2016***; ***Vais et al., 2020***), specifically at $[Ca^{2+}]_m$ ~400 nM. However, as shown in ***Figure 3—figure supplement 1B–C***, I_{Ca} amplitude is unchanged when $[Ca^{2+}]_m$ was set at either Ca^{2+}-free, or 400 nM,

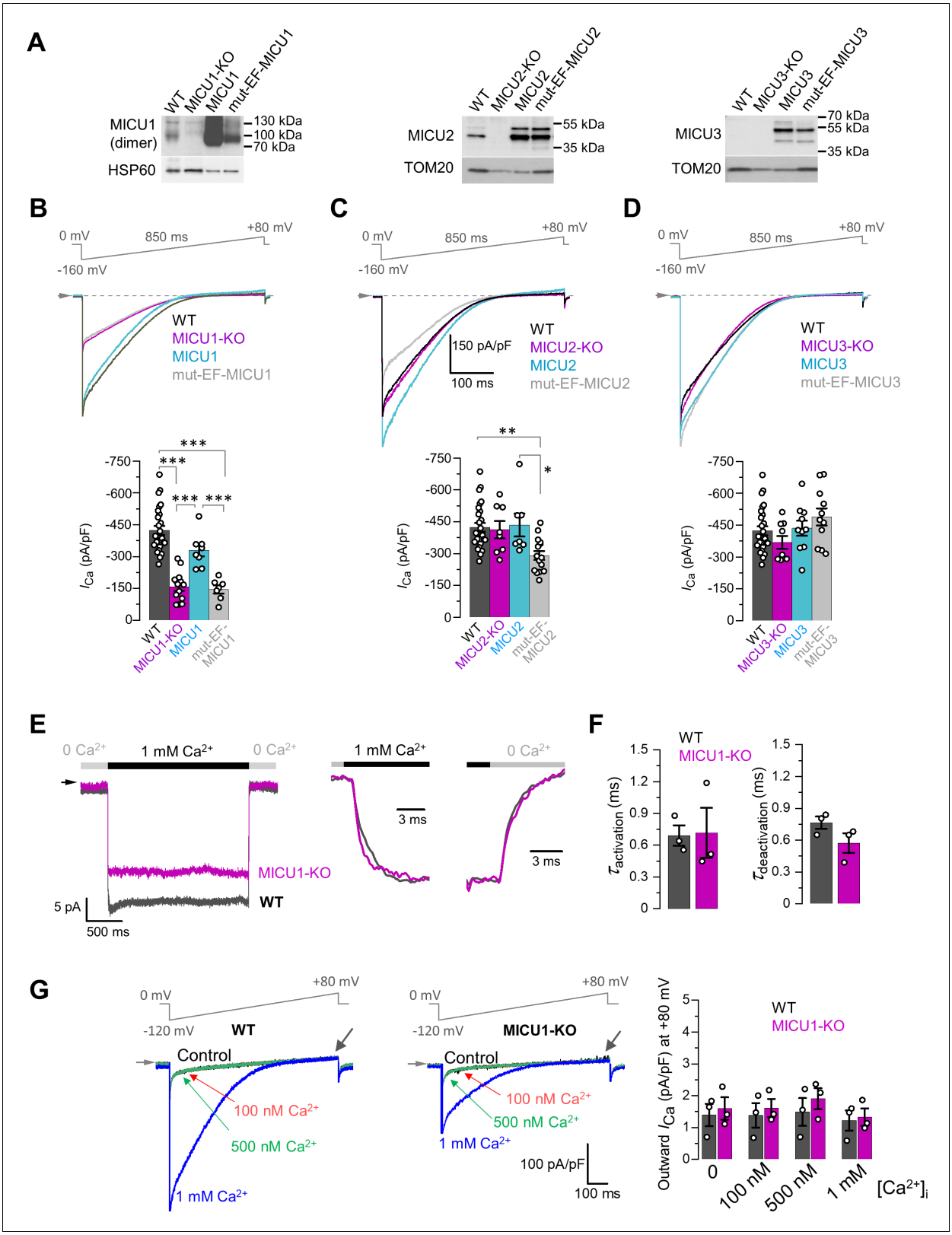

Figure 3. Effects of MICU subunits and their EF hands on the amplitude, kinetics and rectification of I_{Ca}. (**A**) Western blots showing overexpression of MICU subunits or MICU subunits with non-functional EF hands (mut-EF-MICU) in their respective knockout background (*left*, MICU1-KO; *middle*, MICU2-KO and; *right*, MICU3-KO). For MICU1 (*left panel*), samples were prepared without reducing agent, β-mercaptoethanol. The MICU1 band is near the expected molecular weight for the homo- or heterodimer (with MICU2 or 3). (**B–D**) *Upper panels:* I_{Ca} in MICU1-KO (**B**), MICU2-KO (**C**), and MICU3-

Figure 3 continued on next page

Figure 3 continued

KO (**D**) before and after overexpression of a corresponding MICU subunit or its EF hand mutant, as compared to WT. Representative I_{Ca} traces recorded from the mitoplasts of different backgrounds in 1 mM $[Ca^{2+}]_i$ are shown together in a single panel. *Lower panels:* quantification of I_{Ca} amplitudes from the upper panel at −160 mV. The same WT and knockout data were used as in ***Figure 2B***. All superimposed current traces in a panel are compiled from multiple mitoplasts. Data shown as mean ± SEM; one-way ANOVA with post-hoc Tukey test. n = 7–26. (**E**) *Left panel:* I_{Ca} measured at a holding voltage of −100 mV while $[Ca^{2+}]_i$ was rapidly (τ ~0.4 ms, see Materials and methods) switched from virtual zero to 1 mM and then back to virtual zero in WT (*gray*) and MICU1-KO (*purple*) mitoplasts. *Right panel,* I_{Ca} kinetics within ~10 ms after the fast $[Ca^{2+}]_i$ elevation and subsequent decrease in WT (*gray*) and MICU1-KO (*purple*) mitoplasts from the left panel. I_{Ca} traces were normalized to the maximal amplitude to facilitate comparison of kinetics in WT and MICU1-KO. (**F**) *Left:* I_{Ca} activation time constant ($\tau_{activation}$) in WT and MICU1-KO; *Right:* I_{Ca} deactivation time constant ($\tau_{deactivation}$) in WT and MICU1-KO. Data shown as mean ± SEM, n = 3. (**G**) I_{Ca} at $[Ca^{2+}]_m$ = 2 mM and indicated $[Ca^{2+}]_i$ in WT and MICU1-KO. Black arrows point out where the amplitude of outward I_{Ca} was measured. Bar-graph shows the amplitude of outward I_{Ca} measured at +80 mV. All superimposed current traces in a single panel are from the same mitoplast. Data shown as mean ± SEM, n = 3, each $[Ca^{2+}]_i$.
The online version of this article includes the following source data and figure supplement(s) for figure 3:

Source data 1. Raw western blot image for panel A.
Source data 2. Dataset values for ***Figure 3***.
Figure supplement 1. Matrix Ca^{2+} does not regulate I_{Ca}.
Figure supplement 1—source data 1. Raw western blot image for panel A (*Upper*).
Figure supplement 1—source data 2. Raw western blot image for panel A (*Lower*).
Figure supplement 1—source data 3. Dataset values for ***Figure 3—figure supplement 1***.
Figure supplement 2. Fast solution stepping with the solution exchange system.

or 400 µM. Thus, the MCU_{cx} is not regulated by matrix Ca^{2+}, and MICUs only impart the regulation of the MCU_{cx} by cytosolic Ca^{2+}.

Taken together, these data indicate that binding of cytosolic Ca^{2+} to EF hands of MICU subunits allosterically potentiates MCU_{cx} currents.

MICUs regulate the open state probability of MCU_{cx} channel

To investigate the mechanism by which Ca^{2+}-bound MICU subunits potentiate I_{Ca}, we examined the activity of single MCU_{cx} channels in inside-out (matrix-side out) IMM patches (***Figure 4***). Because the unitary MCU_{cx} current (i_{Ca} via a single MCU_{cx} channel) is very small if measured in physiological $[Ca^{2+}]_i$, it must be recorded at high $[Ca^{2+}]_i$ = 105 mM to enable proper resolution (***Kirichok et al., 2004***). As desired for this experiment, using this $[Ca^{2+}]_i$, the EF hand domains of the MICU subunits are fully saturated with Ca^{2+}.

MCU_{cx} exhibits multiple levels of single channel conductance (***Figure 4A–C***; ***Kirichok et al., 2004***). The sub-conductances can be observed at all tested voltages (−40,–80, and −120 mV), but their resolution improves as the transmembrane voltage, and the amplitude of single-channel currents increase. It is clear that the open probability (P_o) of the MCU_{cx} is increased by the hyperpolarization of the IMM as was also shown previously (***Kirichok et al., 2004***). At −120 mV there are full-sized stochastic openings of MCU_{cx} as well as sub-conductance openings at ~80% and ~60% of the amplitude of the fully open i_{Ca} (***Figure 4A–C***). Because similar amplitude levels were observed in all the patches, we conclude that these events represent genuine sub-conductances in the MCU_{cx} channel.

There was no difference in the single channel amplitude between control and MICU1-KO mitoplasts (***Figure 4C***). However, we found that the single-channel open probability (P_o) was significantly decreased ~2–3 fold in MICU1-KO versus WT mitoplasts, depending on the transmembrane voltage (***Figure 4D***). As a result, the time-averaged current contributed by a single MCU_{cx} channel differs significantly between control and MICU1-KO mitoplasts (***Figure 4E***), thus mirroring and explaining the effect of MICU1 knockout on the amplitude of the whole mitoplast I_{Ca} (***Figure 2B***).

We next recorded MCU_{cx} single channel activity using Na^+ as the permeating ion (i_{Na}), in nominally Ca^{2+}-free conditions (MICUs in Ca^{2+}-free state) (***Figure 5A and B***). Similar to our findings with Ca^{2+} as the permeant ion, there were multiple conductance states (i.e. sub-conductances) when Na^+ was the permeant ion. These sub-conductance states were the same in WT and MICU1-KO (***Figure 5C***). However, in contrast to i_{Ca}, there were no significant differences in the open probability of i_{Na} between WT and MICU1-KO when Na^+ was the permeating ion (***Figure 5D***). Accordingly, there was no difference in the time-averaged currents contributed by a single MCU_{cx} channel in

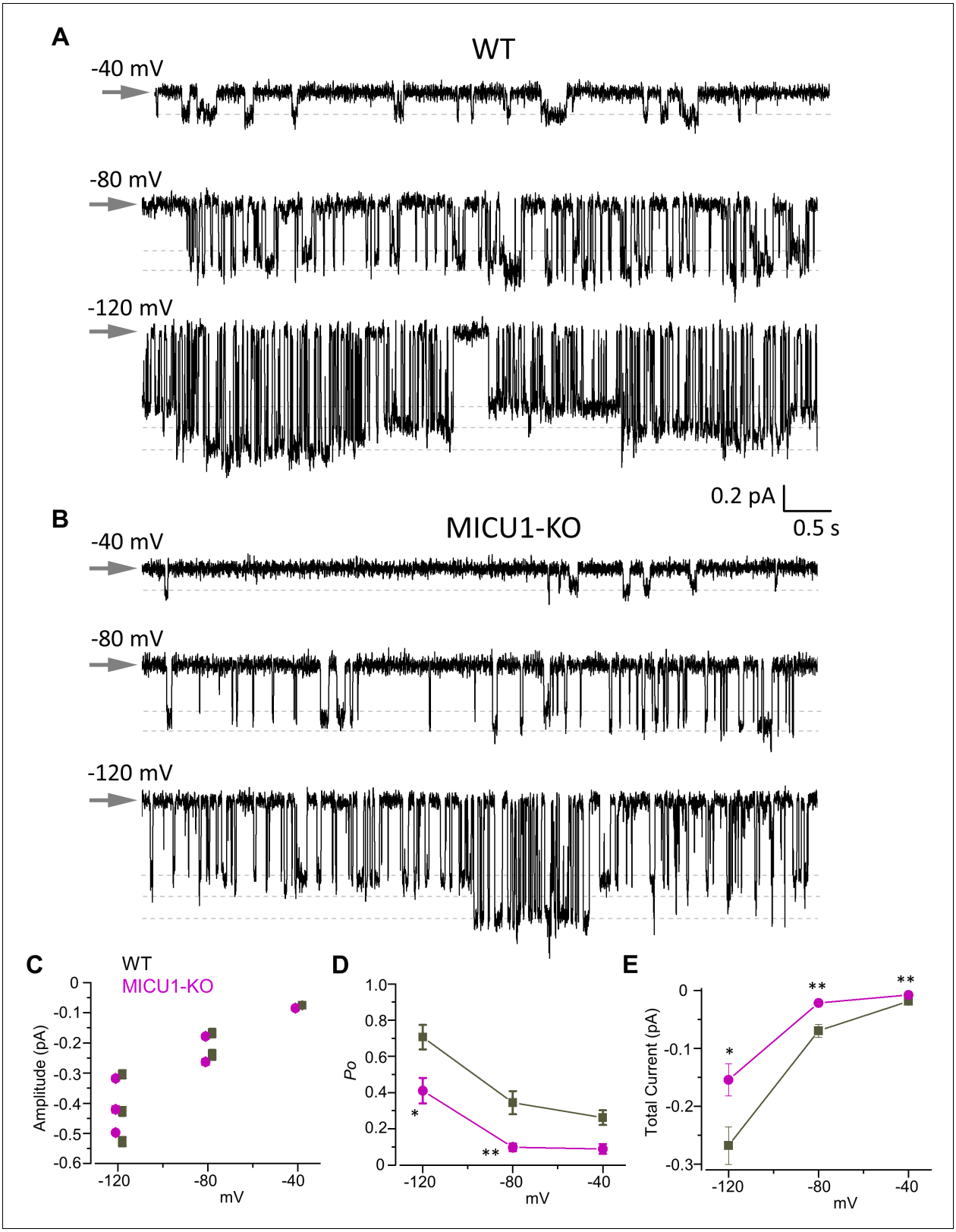

Figure 4. Open probability of the MCU channel in the presence of cytosolic Ca^{2+} is decreased in MICU1-KO. (**A and B**) MCU single-channel Ca^{2+} currents (i_{Ca}) from inside-out IMM patches in WT (**A**) and MICU1-KO (**B**), recorded at indicated potentials in symmetrical 105 mM Ca^{2+}, and low-pass filtered at 0.3 kHz for display purposes. Arrows indicate closed-state level, and downward deflections are the open-state events. Multiple

Figure 4 continued on next page

Figure 4 continued

subconductance levels are clearly visible at −80 and −120 mV. (**C–E**) Single-channel amplitudes (**C**), open probability (P_o) (**D**), and time-averaged unitary current (**E**) (see Methods) in WT and MICU1-KO at indicated potentials. Data shown as mean ± SEM; unpaired t-test, two-tailed, n = 5–6.
The online version of this article includes the following source data for figure 4:

Source data 1. Dataset values for ***Figure 4***.

control and MICU1-KO mitoplasts (***Figure 5E***). This correlates well with the absence of differences in amplitude of the whole mitoplast MCU currents when Na^+ was the permeant ion for these two genotypes (***Figure 2D***).

These results demonstrate that in the Ca^{2+}-bound state, the MICUs potentiate MCU current by increasing the open probability of the MCU/EMRE pore. In the absence of Ca^{2+}, the MICUs do not appear to affect the pore activity.

MCU_{cx} Mn^{2+} conductance

While manganese (Mn^{2+}) is essential for the proper function of several mitochondrial enzymes, its excessive accumulation inhibits oxidative phosphorylation and causes toxicity (***Gunter and Pfeiffer, 1990***). MCU_{cx} appears to be the primary entry pathway for Mn^{2+} entry into mitochondria (***Gunter et al., 2010***). Recently, it has been suggested that MICU1 is responsible for the relatively low permeability of MCU_{cx} for Mn^{2+} as compared to Ca^{2+}, and when MICU1 deficiency or loss-of-function occurs, it can lead to excessive mitochondrial Mn^{2+} accumulation and cellular toxicity (***Kamer et al., 2018***; ***Wettmarshausen et al., 2018***).

We recorded the current carried by Mn^{2+} through MCU_{cx} (I_{Mn}) in the presence of 5 mM $[Mn^{2+}]_i$. I_{Mn} disappeared in MCU-KO and EMRE-KO, confirming that Mn^{2+} current was solely mediated by MCU_{cx} (***Figure 6A–C***). I_{Mn} was significantly smaller (~7-fold) than I_{Ca} via MCU_{cx}, as was also shown previously (***Kirichok et al., 2004***; ***Figure 6D and E***). Interestingly, in MICU1-KO, I_{Mn} and I_{Ca} were reduced to a similar extent (***Figure 6F–H***). Moreover, even the ratio between I_{Mn} and I_{Ca} calculated from the same mitoplast (I_{Mn}/I_{Ca}) was not affected in MICU1-KO (***Figure 6I***). Two important conclusions follow from these observations. First, MICU1 does not differentially regulate I_{Mn} and I_{Ca}. Second, MICU1 potentiates MCU_{cx} in the presence of both Mn^{2+} and Ca^{2+}. These results are in contrast to a popular model in which MICUs occlude MCU_{cx}, and that this occlusion is relieved only by Ca^{2+} but not by Mn^{2+} (***Kamer et al., 2018***; ***Wettmarshausen et al., 2018***). However, our results are in agreement with important earlier studies which found that cytosolic Mn^{2+} allosterically stimulates mitochondrial Ca^{2+} uptake just like Ca^{2+} (***Allshire et al., 1985***; ***Hughes and Exton, 1983***; ***Kröner, 1986***; ***Vinogradov and Scarpa, 1973***).

We further sought to explain why I_{Mn} via MCU_{cx} is smaller than I_{Ca}. In the presence of Mn^{2+}, I_{Ca} was decreased (***Figure 6E***). This decrease was the same in MICU1-KO demonstrating that it was a pore effect (***Figure 6F and J***). This suggests that Mn^{2+} slows down Ca^{2+} permeation simply because it dwells in the pore longer than Ca^{2+} due to tighter binding (***Lansman et al., 1986***). The higher affinity of Mn^{2+} to the pore and the longer dwell time also explains why I_{Mn} is smaller than I_{Ca}.

Thus, the I_{Ca} and I_{Mn} phenotypes of MICU1-KO are the same, and MICU1 does not determine the preference of MCU_{cx} for Ca^{2+} over Mn^{2+}. Permeation of both Ca^{2+} and Mn^{2+} is enhanced, rather than inhibited by MICU1.

Mg^{2+} occludes the MCU_{cx} pore independently of MICU1

Mg^{2+}, the most abundant cytosolic divalent ion, is an important negative regulator of MCU_{cx}-mediated mitochondrial Ca^{2+} uptake (***Gunter et al., 2010***; ***Hutson et al., 1976***). However, the mechanism of the inhibitory action of Mg^{2+} on MCU_{cx} is poorly understood. Our previous study suggested that in Ca^{2+}-free conditions, Mg^{2+} occludes the MCU_{cx} pore for Na^+ permeation (***Kirichok et al., 2004***). Here, we investigate how Mg^{2+} affects Ca^{2+} conduction through MCU_{cx}.

We first studied how cytosolic Mg^{2+} affects activation of I_{Ca} by $[Ca^{2+}]_i$ (***Figure 7A and B***). The results of these experiments clearly demonstrated that I_{Ca} is inhibited in the presence of Mg^{2+}, and that this inhibition was primarily prominent in the lower range of micromolar $[Ca^{2+}]_i$ (***Figure 7B***). Thus, we specifically tested the effect of $[Mg^{2+}]_i$ in this range of $[Ca^{2+}]_i$ by recording I_{Ca} at 30 µM $[Ca^{2+}]$. In these experiments, we found that I_{Ca} in the WT MCU_{cx} remains about double the I_{Ca} in

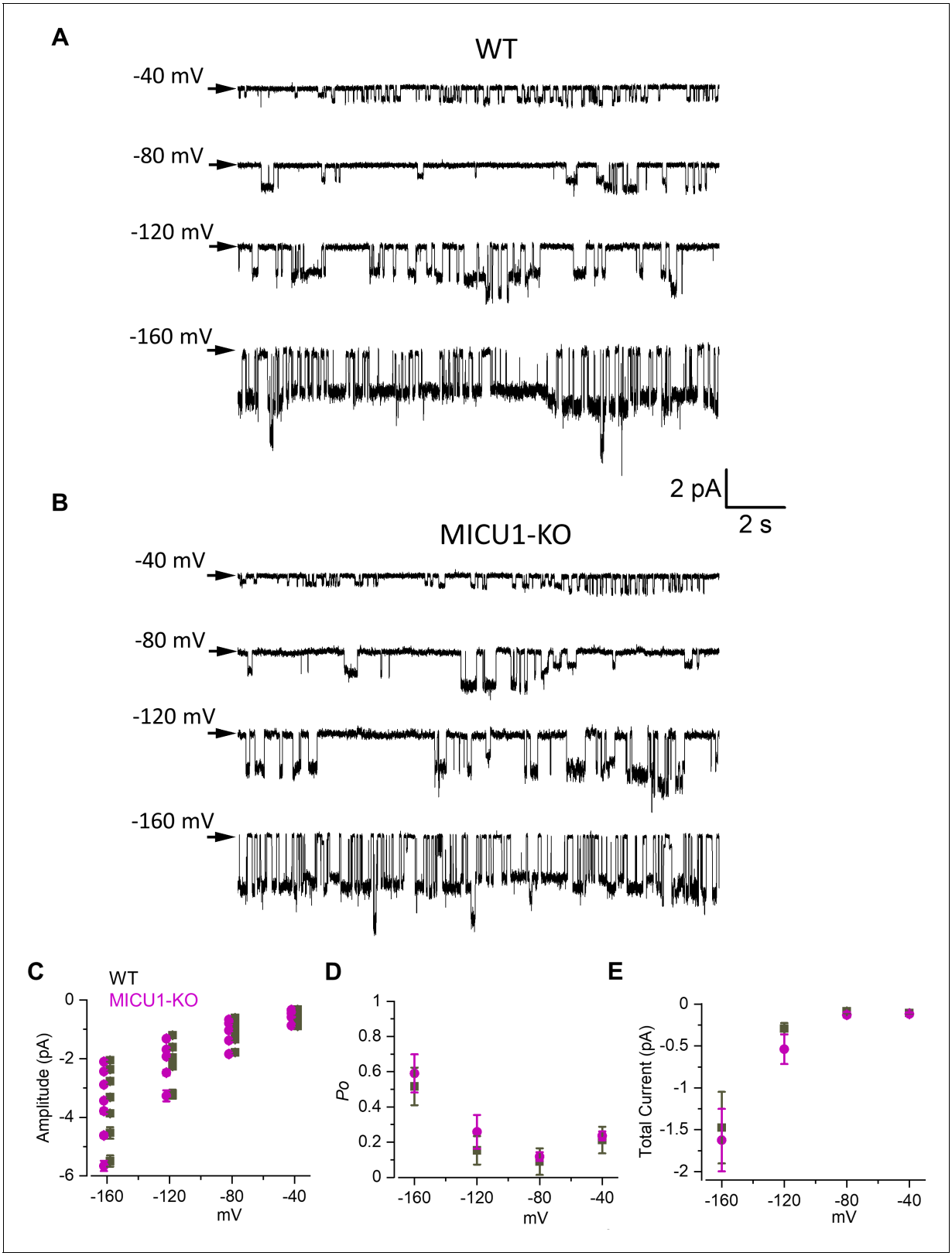

Figure 5. Open probability of the MCU channel in the absence of Ca^{2+} remains unchanged in MICU1-KO. (**A and B**) MCU single-channel Na^+ currents (i_{Na}) from inside-out IMM patches in WT (**A**) and MICU1-KO (**B**), recorded at indicated potentials in symmetrical 150 mM Na^+, and low-pass filtered at 0.3 kHz for display purposes. Arrows indicate closed-state level, and downward deflections are the open-state events. Multiple subconductance levels

Figure 5 continued on next page

Figure 5 continued

are clearly visible at all potentials. (**C–E**) Single-channel amplitudes (**C**), open probability (P_o) (**D**), and time-averaged unitary current (**E**) (see Methods) in WT and MICU1-KO at indicated potentials. Data shown as mean ± SEM; unpaired t-test, two-tailed, n = 6–7.

The online version of this article includes the following source data for figure 5:

Source data 1. Dataset values for ***Figure 5***.

MICU1-KO whether [Mg^{2+}] is 200 µM or 0 (***Figure 7C***). Thus, these data suggest that the potentiating effect that MICU1 exerts on MCU_{cx} does not depend on [Mg^{2+}]. Furthermore, as shown in ***Figure 7D***, Mg^{2+} inhibits I_{Ca} with similar IC_{50} in WT (149 ± 20 µM) and MICU1-KO (156 ± 20 µM). Taken together, these findings indicate that Mg^{2+} exerted its inhibitory effect at the MCU_{cx} pore (***Figure 7C and D***) and not through the MICUs. The pronounced competitive nature of the Mg^{2+} inhibition (***Figure 7B***) suggests that Mg^{2+} binds within the MCU_{cx} selectivity filter formed by Asp and Glu residues (***Baradaran et al., 2018***; ***Fan et al., 2018***; ***Nguyen et al., 2018***; ***Yoo et al., 2018***). Mg^{2+} is a smaller divalent cation than Ca^{2+}, and it is more difficult for Mg^{2+} to shed its hydration shell to fit into a narrow high-affinity Ca^{2+} binding site formed by Glu (site 2). However, Mg^{2+} could bind to the outermost and wider Asp binding site (site 1) of the selectivity filter even with a hydration shell. Such Mg^{2+} binding would not allow Mg^{2+} permeation, but would occlude the pore.

In conclusion, Mg^{2+} is an MCU_{cx} pore blocker that at the resting [Ca^{2+}]$_i$, would strongly compete with Ca^{2+} for binding to the selectivity filter, limiting Ca^{2+} permeation. The Mg^{2+} occlusion of the MCU_{cx} pore can at least partially explain low mitochondrial Ca^{2+} uptake at resting [Ca^{2+}]$_i$.

Discussion

In summary, we demonstrate that the primary function of MICU subunits is to potentiate the activity of the MCU_{cx} as cytosolic Ca^{2+} is elevated and binds to MICU's EF hands. This potentiation would result in efficient stimulation of the mitochondrial ATP production in response to cytosolic Ca^{2+} signaling events, when energy demand is increased as shown in neurons (***Ashrafi et al., 2020***) and heart (***Wescott et al., 2019***). Although at low [Ca^{2+}]$_i$, MICU1-KO mitochondria appear to have higher Ca^{2+} uptake in comparison to WT, we find no evidence of a plug that blocks ion permeation via MCU_{cx}. On the other hand, at high [Ca^{2+}]$_i$, the uptake was lower in MICU1-KO, which we demonstrate by the patch clamp analysis is due to loss of MICU-mediated potentiation of MCU_{cx}. Mechanistically, at low [Ca^{2+}]$_i$ the MCU_{cx} channel is open in a lower open probability mode, but as [Ca^{2+}]$_i$ is elevated, MICUs increase MCU_{cx} open state probability, potentiating its activity (***Figure 6K***). MICUs are likely to achieve this effect by interacting with EMRE that is predicted to control the gating of the MCU pore (***Wang et al., 2019***; ***Fan et al., 2020***; ***Wang et al., 2020b***; ***Zhuo et al., 2021***). We also show that the inward rectification property of MCU_{cx} is independent of MICUs. Lastly, in contrast to the previous report (***Vais et al., 2016***), we found no evidence for the regulation of MCU_{cx} activity by matrix [Ca^{2+}].

Regulation of MCU_{cx} function by cytosolic [Ca^{2+}]

Assuming that K_d for Ca^{2+} binding to MICU EF hands is ~600 nM (***Kamer et al., 2017***), MICUs would exert their potentiating effect over a broad range of physiological [Ca^{2+}]$_i$ that range from resting to low micromolar. By doing so, MICUs can help the MCU_{cx} to overcome the mitochondrial Ca^{2+} efflux machinery and to elevate [Ca^{2+}]$_m$ to achieve adequate stimulation of the mitochondrial ATP production. In previous reports, there has been significant inconsistency as to the proposed effect of MICU1 on mitochondrial Ca^{2+} uptake at high [Ca^{2+}]$_i$ (***Supplementary file 1a and b***). For example, mitochondrial Ca^{2+} uptake rate appears to be decreased in isolated liver mitochondria from mice following siRNA-mediated knockdown of MICU1 or MICU2 in an earlier study (***Plovanich et al., 2013***). Another study (***Csordás et al., 2013***) also showed decreased uptake rates when MICU1 was knocked down in HeLa cells and hepatocytes leading authors to propose that MICU1 contributes to the cooperative activation of MCU_{cx}, but the effect was mild and it disappeared in the absence of Mg^{2+}. On the other hand, many reports (***Kamer et al., 2018***; ***Logan et al., 2014***; ***Mallilankaraman et al., 2012a***; ***Vais et al., 2016***) showed no change in MCU activity upon MICU1 loss at high [Ca^{2+}]$_i$ but only alteration in the threshold for mitochondrial Ca^{2+} uptake. However, a recent study again showed a decrease in Ca^{2+} uptake in isolated liver mitochondria in MICU1-KO

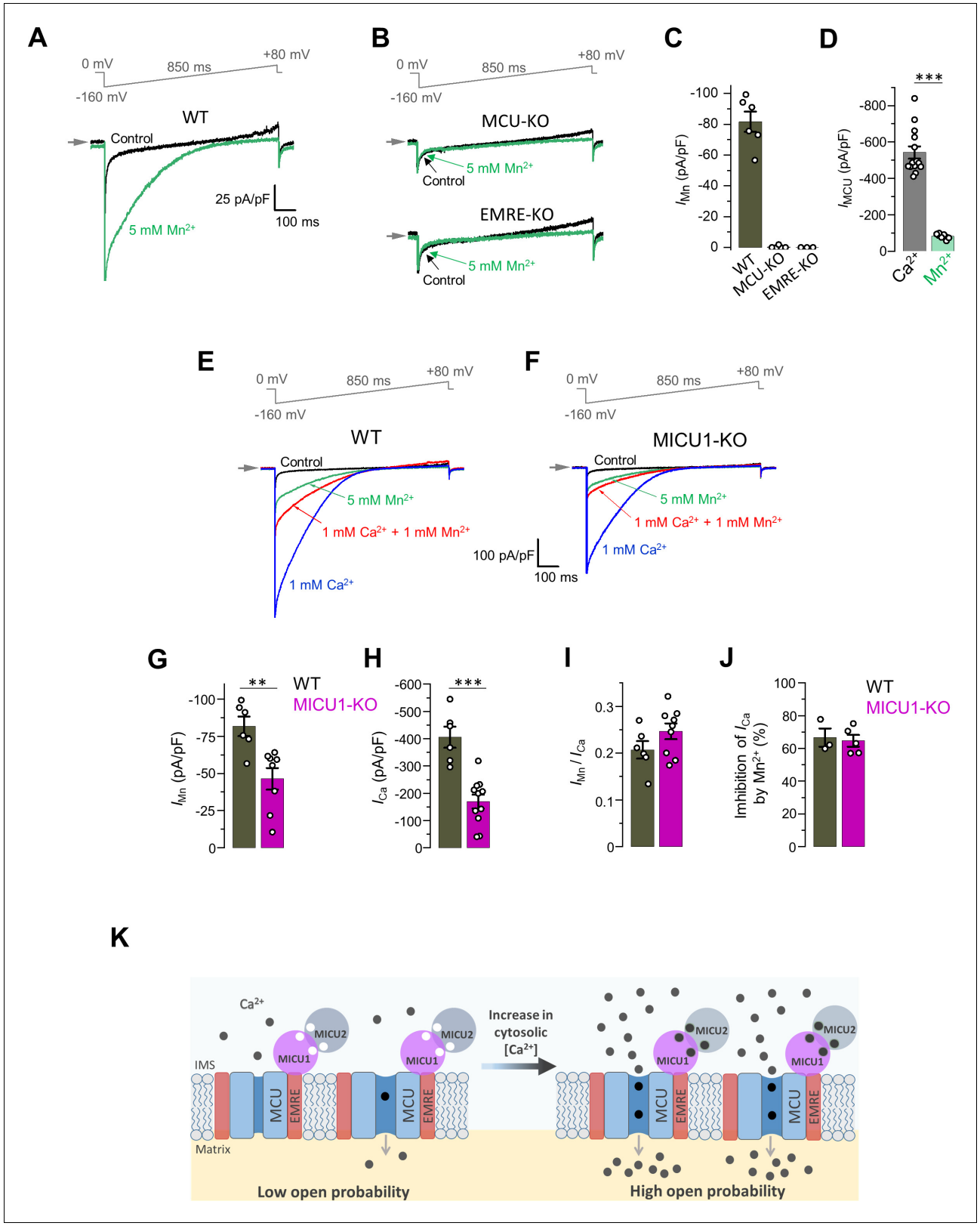

Figure 6. I_{Mn} is reduced in MICU1-KO to the similar extent as I_{Ca}. (**A and B**) Representative inward I_{Mn} in WT (**A**), MCU-KO (*upper panel*) and EMRE-KO (*lower panel*, **B**) mitoplasts at 5 mM $[Mn^{2+}]_i$. All superimposed current traces in a single panel are from the same mitoplast. (**C**) I_{Mn} measured at −160 mV from WT, MCU-KO and EMRE-KO mitoplasts. Data shown as mean ± SEM. (n = 3–6). (**D**) MCU current amplitude (I_{MCU}) in the presence of 5 mM $[Ca^{2+}]_i$ and 5 mM $[Mn^{2+}]_i$ in WT mitoplasts. Currents were measured at −160 mV. Data shown as mean ± SEM; unpaired t-test, two-tailed. n = 6–14. (**E**

Figure 6 continued on next page

Figure 6 continued

and F) Representative I_{Ca} (*blue*, $[Ca^{2+}]_I$ = 1 mM), I_{Mn} (*green*, $[Mn^{2+}]_I$ = 5 mM) and inhibition of I_{Ca} by Mn^{2+} (*red*, $[Ca^{2+}]_I$ = 1 mM and $[Mn^{2+}]_I$ = 1 mM) as recorded from the same mitoplast in WT (**E**) and MICU1-KO (**F**). All superimposed current traces in a single panel are from the same mitoplast. (**G–J**) I_{Mn} (**G**), I_{Ca} (**H**), I_{Mn}/I_{Ca} ratio (I, measured in the same mitoplast), and inhibition of I_{Ca} by 1 mM $[Mn^{2+}]_i$ (**J**) in WT and MICU1-KO. Data shown as mean ± SEM; unpaired t-test, two-tailed, n = 3–11. (**K**) Proposed model of the MCU complex gating and the role of MICU subunits in Ca^{2+}-dependent potentiation of the MCU current. The MCU complex is a constitutively active channel and the level of its activity is determined by the probability of open state (P_o). At resting $[Ca^{2+}]_i$, P_o is low. As $[Ca^{2+}]_i$ is increased and Ca^{2+} binds to the EF hands of MICU subunits, MICUs increase P_o, resulting in the increase in the MCU activity.

The online version of this article includes the following source data for figure 6:

Source data 1. Dataset values for ***Figure 6***.

mouse relative to WT (***Liu et al., 2016***). This correlates well with our data showing direct potentiation of the MCU_{cx} activity by MICU1. Thus, the potentiating effect of MICUs on the MCU_{cx} was discernible in the previous research but was largely rejected due to the predominant view that the primary function of MICUs is to occlude the MCU_{cx} pore.

Our data is incompatible with the model in which MICUs occlude the MCU pore at low $[Ca^{2+}]_i$ and impart a $[Ca^{2+}]_i$ activation threshold on the MCU_{cx}. This model explains the increase of

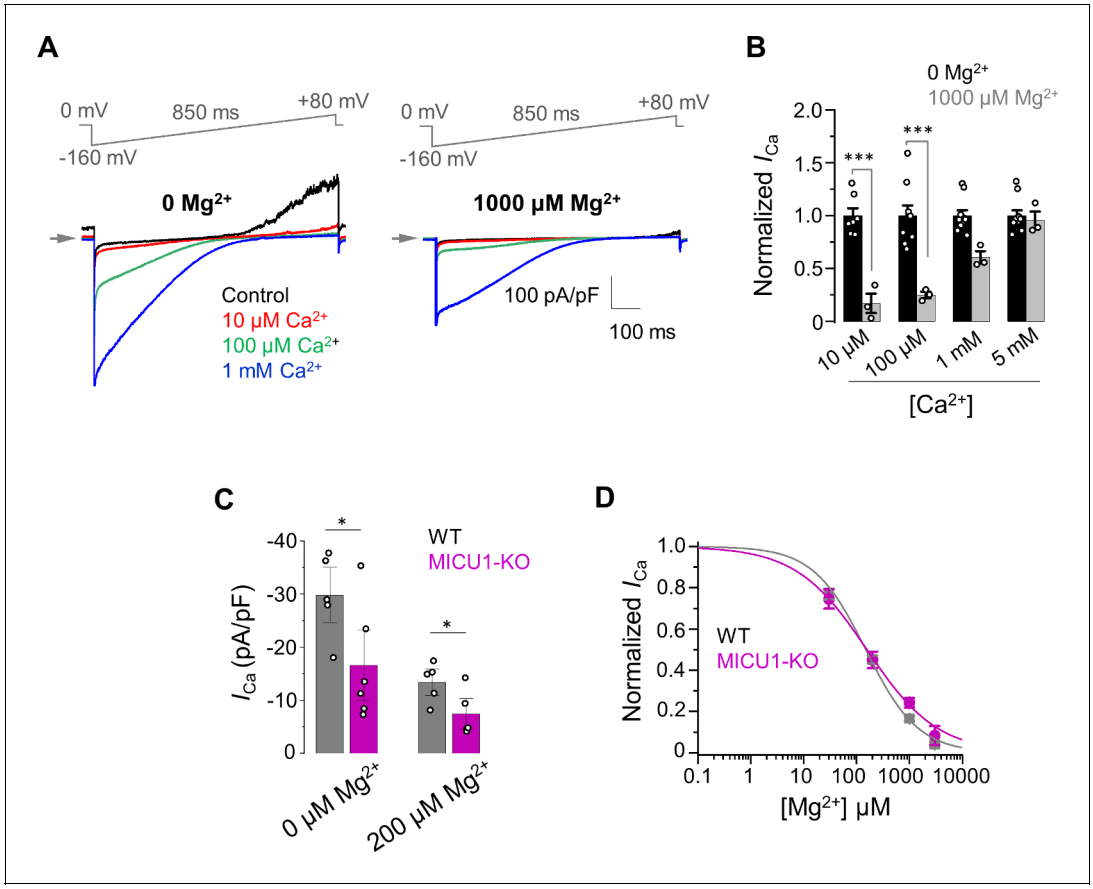

Figure 7. The inhibitory effect of Mg^{2+} on MCU_{cx} does not depend on MICU1. (**A**) Inward I_{Ca} elicited at indicated $[Ca^{2+}]_i$ in the presence of 0 (*left*) and 1000 µM (*right*) $[Mg^{2+}]_i$ in WT mitoplasts. (**B**) I_{Ca} elicited at indicated $[Ca^{2+}]_i$ in the presence of 0 and 1000 µM $[Mg^{2+}]_i$. I_{Ca} amplitudes were measured at −160 mV in WT mitoplasts and normalized per I_{Ca} at $[Mg^{2+}]_i$ = 0. Mean ± SEM; unpaired t-test, two-tailed. (**C**) Quantification of I_{Ca} elicited at 30 µm $[Ca^{2+}]_i$ in the presence of 0 and 200 µM $[Mg^{2+}]_i$ in WT and MICU1-KO. Currents were measured at −160 mV. Data shown as mean ± SEM; unpaired t-test, two-tailed, n = 5–6. (**D**) Dose-response curve of I_{Ca} inhibition by $[Mg^{2+}]_i$ in WT (IC_{50} = 149 ± 20 µM, n_H = 0.9 ± 0.1; n = 5) and MICU1-KO (IC_{50} = 156 ± 21 µM, n_H = 0.7 ± 0.1; n = 4). Mean ± SEM; unpaired t-test, two-tailed.

The online version of this article includes the following source data for figure 7:

Source data 1. Dataset values for ***Figure 7***.

mitochondrial Ca^{2+} accumulation at resting $[Ca^{2+}]_i$ in MICU1-KO to 'unblocking' of MCU_{cx}. However, in this concentration range, the MCU_{cx} activity is so slow that the mitochondrial Ca^{2+} accumulation is definitely influenced by many other factors. Among other possibilities, one can speculate that mitochondrial Ca^{2+} efflux, matrix Ca^{2+} buffering, matrix pH and permeability of the outer mitochondrial membrane might be altered in MICU1-KO to facilitate mitochondrial Ca^{2+} accumulation at low $[Ca^{2+}]_i$.

Because these multiple factors can be affected by MICU1-KO differently in different experimental system and conditions, the change in the threshold can vary from one system to another. In *Trypanosoma cruzi*, where the composition of the MCU complex (including EMRE and MICU1) is similar to mammals, MICU1 knockout causes an increase in the Ca^{2+} uptake 'threshold' and a marked decrease in Ca^{2+} uptake capacity at all $[Ca^{2+}]_i$ (**Bertolini et al., 2019**). A recent report also found no apparent $[Ca^{2+}]_i$ threshold for MCU in isolated mitochondria from heart and skeletal muscle (**Wescott et al., 2019**). Similarly sympathetic neurons lack a discernible threshold and mitochondria were shown to accumulate small amount of Ca^{2+} at $[Ca^{2+}]_i$ levels as low as 200 nM (**Colegrove et al., 2000a**; **Colegrove et al., 2000b**). Finally, interpretation of the MICU1-KO phenotypes can be further complicated by possible functional roles of MICU1 outside of the MCU complex (**Gottschalk et al., 2019**; **Tomar et al., 2019**; **Tufi et al., 2019**). In particular, MICU1 was proposed to interact with the MICOS complex, affecting the cristae structure (**Tomar et al., 2019**).

Examination of the conduction pathway of the MCU_{CX}

To circumvent the problem of isolating the MCU_{cx} activity from the other mitochondrial Ca^{2+} homeostatic mechanisms, we leveraged the capacity of MCU_{cx} to conduct Na^+. The Na^+ permeation via MCU_{cx} is observed not only in isolated mitoplasts but also in intact mitochondria. Na^+ permeates via MCU_{cx} because Ca^{2+} and Na^+ ions have the same ionic diameter, and Na^+ can pass through Ca^{2+} channels when Ca^{2+} is removed from the selectivity filter (**Hess and Tsien, 1984**; **Hess et al., 1986**; **Tang et al., 2014**). Ca^{2+} binds to the MCU_{cx} selectivity filter with an exceptionally high affinity ($K_d \leq 2$ nM) (**Kirichok et al., 2004**), and re-addition of cytosolic Ca^{2+} leads to I_{Na} inhibition upon Ca^{2+} binding to this site. Importantly, MICUs are not involved in this inhibition, as it is not affected by MICU1-KO (**Figure 2—figure supplement 2**). In intact mitochondria, Na^+ uptake via WT or MICU1-deficient MCU_{cx} causes the same $\Delta\Psi$ depolarization, demonstrating that at low $[Ca^{2+}]_i$ MCU_{cx} is not occluded regardless of its association with MICUs. Moreover, using mitochondrial patch-clamp under Ca^{2+}-free conditions, we recorded a robust I_{Na} via MCU, and the amplitude of this I_{Na} was not affected in MICU1-KO. This demonstrates that MCU pore is not occluded by MICUs at low $[Ca^{2+}]_i$.

The complexity of the MCU_{cx} presents formidable difficulties even for the direct electrophysiological analysis. The electrophysiological phenotypes observed may be associated with altered expression levels of other subunits rather than the loss of MICU1. We not only analyzed the expression levels of all MCU complex subunits (**Figure 2—figure supplement 1D–F**) but also measured I_{Ca}/I_{Na} ratio in the same mitoplast (**Figure 2C–F**) to ensure that we correctly capture the role of MICU1 in the MCU complex.

Cryo-EM studies and the dynamic function of MICUs

Recently, cryo-EM structures of the MCU_{cx} holocomplex reveal that it is composed of two conjoined MCU/EMRE pores with a MICU1/MICU2 heterodimer attached to each of them (**Fan et al., 2020**; **Wang et al., 2020b**; **Zhuo et al., 2021**). Based on molecular weight of the MCU_{cx} as observed on the Blue native PAGE (**Sancak et al., 2013**), this structure likely represents the complete MCU_{cx} of intact mitochondria. This is the primary structural form of MCU_{cx} in the mitochondrial inner membrane.

However, in addition to this complete MCU_{cx}, the cryo-EM analysis also reported structures of a monomeric MCU/EMRE pore with a single MICU1/MICU2 heterodimer. Although this does not appear to be the predominant state of the native MCU_{cx}, it was primarily used for the analysis of the interaction between the pore and the MICU1/MICU2 dimer. Based on this analysis, a conclusion was made that in the absence of Ca^{2+}, MICU1/MICU2 dimer occluded the MCU_{cx} pore. Wang et al. (**Wang et al., 2020b**) observed occlusion of the dimeric complex, but such MICU1-occluded dimeric complex represented only ~10% of the total number of analyzed particles in the absence of Ca^{2+}.

The low prevalence of the dimeric complexes can be purely due to the experimental limitations, but a more thorough analysis of occlusion in this native form of MCU_{cx} is warranted. At the same time, another work that analyzed the complete MCU_{cx} with two pores and two MICU1/MICU2 heterodimers, did not show any occlusion (**Zhuo et al., 2021**). In this structure, the two MICU1/MICU2 heterodimers interact between each other, leaving both pores unoccluded (**Zhuo et al., 2021**). As more MCU_{cx} structural data appear in the future, it is important to take into consideration the completeness of the complex and the new functional data on the MICU subunits presented here.

We are at the very beginning of the structural characterization of MCU_{cx}. As this crucial work continues, selection of the experimental conditions is key to understanding how the channel works under physiological conditions. As we emphasize here, the direct inhibitory effect of Mg^{2+} on the MCU pore is important but has not yet been taken into consideration. In fact, Mg^{2+} was omitted in all structural studies of MCU_{cx} holocomplex (**Fan et al., 2020**; **Wang et al., 2020b**; **Zhuo et al., 2021**). As we discussed before, Mg^{2+} is likely to bind to the same Asp ring of the selectivity filter where MICU1 was predicted to bind and, may therefore significantly affect conformational states of MCU_{cx}. Thus, to determine how MICU1 interacts with the MCU_{cx} pore, structural studies should be performed under conditions that include physiological concentrations of Mg^{2+}. Furthermore, occlusion of the MCU/EMRE pore by MICUs in the absence of Ca^{2+} was observed when the cryoEM particles were obtained in a solution that had ionic strength ~three times lower than physiological (**Fan et al., 2020**; **Wang et al., 2020b**). In contrast, the unoccluded state was observed at the physiological ionic strength (**Zhuo et al., 2021**). This difference is critical, because the occlusion of the MCU pore by MICU1 strongly depends on ionic interactions (**Fan et al., 2020**; **Wang et al., 2020b**). Another important consideration is the presence of cardiolipin in MCU_{cx} structures, likely affected by the type of detergent used during purification. Interestingly, the occluded state was observed in the structures that contained no cardiolipin (**Fan et al., 2020**; **Wang et al., 2020b**), while the unoccluded MCU_{cx} structure contained cardiolipin (**Zhuo et al., 2021**). This point is important as cardiolipin interacts with the MCU complex (**Ghosh et al., 2020**; **Zhuo et al., 2021**) and may regulate MICU function (**Kamer and Mootha, 2014**).

In conclusion, we find no evidence for the occlusion of the MCU_{cx} pore by MICUs at resting $[Ca^{2+}]_i$. Instead, under these conditions MCU_{cx}-mediated uptake is limited by the low concentration of the conducting ion and by the Mg^{2+} block. A slow mitochondrial Ca^{2+} uptake at resting $[Ca^{2+}]_i$ is likely at balance with the Ca^{2+} efflux mechanisms, which prevents mitochondrial Ca^{2+} overload (**Nicholls, 2005**). On the other hand, the phenomenon of allosteric potentiation of MCU_{cx} has been known for many decades (**Gunter et al., 2010**; **Kröner, 1986**), and this work provides its clear mechanistic explanation.

Materials and methods

Key resources table

Reagent type (species) or resource	Designation	Source or reference	Identifiers	Additional information
Cell line (*M. musculus*)	DRP1-KO (*Dnm1l*$^{-/-}$) (Mouse embryonic fibroblast)	**Ishihara et al., 2009**		Cell line maintained in D. Chan and K. Mihara lab; *Dnm1l*$^{-/-}$ background
Cell line (*M. musculus*)	WT (*Dnm1l*$^{+/+}$) (Mouse embryonic fibroblast)	**Liu et al., 2016**		Cell line maintained in T. Finkel lab; *Dnm1l*$^{+/+}$ background
Cell line (*M. musculus*)	MICU1-KO (*Micu1*$^{-/-}$) (Mouse embryonic fibroblast)	**Liu et al., 2016**		Cell line maintained in T. Finkel lab; *Dnm1l*$^{+/+}$ background
Cell line (*M. musculus*)	MCU-KO (*Mcu*$^{-/-}$) (Mouse embryonic fibroblast)	This paper		Cell line maintained in Y. Kirichok and V. Garg lab. *Dnm1l*$^{-/-}$ background
Cell line (*M. musculus*)	EMRE-KO (*Smdt1*$^{-/-}$) (Mouse embryonic fibroblast)	This paper		Cell line maintained in Y. Kirichok and V. Garg lab. *Dnm1l*$^{-/-}$ background

Continued on next page

Continued

Reagent type (species) or resource	Designation	Source or reference	Identifiers	Additional information
Cell line (*M. musculus*)	MICU1-KO (*Micu1*$^{-/-}$) (Mouse embryonic fibroblast)	This paper		Cell line maintained in Y. Kirichok and V. Garg lab. *Dnm1l*$^{-/-}$ background
Cell line (*M. musculus*)	MICU2-KO (*Micu2*$^{-/-}$) (Mouse embryonic fibroblast)	This paper		Cell line maintained in Y. Kirichok and V. Garg lab. *Dnm1l*$^{-/-}$ background
Cell line (*M. musculus*)	MICU3-KO (*Micu3*$^{-/-}$) (Mouse embryonic fibroblast)	This paper		Cell line maintained in Y. Kirichok and V. Garg lab. *Dnm1l*$^{-/-}$ background
Strain, strain background (*M. musculus*)	MCU-KO (*Mcu*$^{-/-}$) mouse	This paper		Mouse line maintained in T. Finkel lab
Recombinant DNA Reagent	*Mcu* (plasmid)	This paper		Lentiviral Construct (Y. Kirichok and V. Garg lab)
Recombinant DNA Reagent	*Smdt1* (alias *Emre*) (plasmid)	This paper		Lentiviral Construct (Y. Kirichok and V. Garg lab)
Recombinant DNA Reagent	*Micu1* (plasmid)	This paper		Lentiviral Construct (Y. Kirichok and V. Garg lab)
Recombinant DNA Reagent	*Micu2* (plasmid)	This paper		Lentiviral Construct (Y. Kirichok and V. Garg lab)
Recombinant DNA Reagent	*Micu3* (plasmid)	This paper		Lentiviral Construct (Y. Kirichok and V. Garg lab)
Recombinant DNA Reagent	*mut-EF-Micu1* (plasmid)	This paper		Lentiviral Construct (Y. Kirichok and V. Garg lab)
Recombinant DNA Reagent	*mut-EF-Micu2* (plasmid)	This paper		Lentiviral Construct (Y. Kirichok and V. Garg lab)
Recombinant DNA Reagent	*mut-EF-Micu3* (plasmid)	This paper		Lentiviral Construct (Y. Kirichok and V. Garg lab)
Recombinant DNA Reagent	*Cepia2mt* (plasmid)	***Suzuki et al., 2014***. Lentiviral construct was made in this paper.		Lentiviral construct
Antibody	MCU antibody (rabbit polyclonal)	Sigma	HPA016480; RRID:AB_2071893	WB (1:2000)
Antibody	EMRE antibody (mouse monoclonal)	Santa Cruz	sc-86337; RRID:AB_2250685	WB (1:200)
Antibody	MICU1 antibody (rabbit polyclonal)	Cell Signalling	D4P8Q (12524S); RRID:AB_2797943	WB (1:2000)
Antibody	MICU2 antibody (mouse monoclonal)	Bethyl laboratories	A300-BL19212	WB (1:500)
Antibody	MICU3 antibody (mouse monoclonal)	Sigma	HPA024779; RRID:AB_1848023	WB (1:1000)
Antibody	VDAC antibody (rabbit monoclonal)	Santa Cruz	ab15895; RRID:AB_2214787	WB (1:1000)
Antibody	TOM20 antibody (rabbit polyclonal)	Santa Cruz	sc-11415; RRID:AB_2207533	WB (1:2000)
Antibody	HSP60 antibody (rabbit polyclonal)	Santa Cruz	sc-1052; RRID:AB_631683	WB (1:3000)
Chemical compound, drug	ANTI-FLAG M2 Affinity Gel	Sigma-Aldrich	Cat# A2220; RRID:AB_10063035	

Continued on next page

Continued

Reagent type (species) or resource	Designation	Source or reference	Identifiers	Additional information
Software, algorithm	PClamp 10	Molecular Devices		https://www.moleculardevices.com/systems/conventional-patch-clamp/pclamp-10-software
Software, algorithm	Origin 7.5	OriginLab		http://www.originlab.com/
Software, algorithm	ImageJ Software	ImageJ		https://imagej.net/
Software, algorithm	$[Ca^{2+}]_m$ threshold detection algorithm	Custom-made		https://github.com/ishanparanjpe/upstroke (**Paranjpe et al., 2019**)

Contact for reagent and resource sharing

Further information and requests for reagents may be directed to and will be fulfilled by Lead Contact Yuriy Kirichok (yuriy.kirichok@ucsf.edu).

Experimental model

Cell culture and recombinant gene expression

All mouse embryonic fibroblast (MEF) cells with (**Liu et al., 2016**) or without Drp1 (**Ishihara et al., 2009**), and all knockout clones were grown in low glucose (5.6 mM) Dulbecco's modified Eagle's medium (DMEM) supplemented with 10% FBS, 100 U/ml penicillin, and 100 U/ml streptomycin at 37˚C, 5% CO_2. Cells were maintained by splitting every 48–72 hr at a ratio of 1:5 to 1:10. The MEF cell lines were authenticated by short tandem repeat profiling conducted by Labcorp. The cell lines were free of mycoplasma as determined by PCR based detection (**Dreolini et al., 2020**).

We used third-generation lentiviral (bi-cistronic) vectors containing the ORF for gene of interest with or without a selection marker (EGFP, mCherry or puromycin). The vectors were generated by VectorBuilder, Inc (Chicago, IL, USA), and their sequences were confirmed independently by the company and by us. Recombinant cDNA expressing cells were enriched using multiple rounds of FACS or antibiotic selection. In some cases, EGFP was targeted to mitochondria (using a mitochondrial targeting sequence from COX8) to identify mitoplasts expressing the recombinant protein of interest during patch clamp experiments.

Animals

Mice were maintained on a standard rodent chow diet under 12 hr light and dark cycles. All animal experiments were performed with male mice (2–5 month old) according to procedures approved by the UCSF Institutional Animal Care and Use Committee and adhered to NIH standards. C57BL/6J were obtained from the Jackson laboratory. MCU-KO mice were obtained from Dr. Torren Finkel and have been used previously (**Pan et al., 2013**).

Method details

Gene expression analysis (qRT-PCR) qPCR was performed by Syd Labs (Natick, MA, USA). Total RNA was isolated from cells using the RNAeasy Minikit (QIAGEN), and reverse transcribed using the First Strand cDNA Synthesis Kit (Syd Labs). qPCR reactions were performed with the following gene-specific primers (generated by Integrated DNA Technologies):

Hprt, Forward Primer 5'-GTCCCAGCGTCGTGATTAGC-3'
Reverse Primer 5'-GTGATGGCCTCCCATCTCCT-3'
Mcu, Forward Primer 5'-AAGGGCTTAGCGAGTCTTGTC-3'
Reverse Primer 5'- GGGTGCTGGTGTGTTAGTGT –3'
Mcub, Forward Primer 5'-CCACACCCCAGGTTTTATGTATG-3'
Reverse Primer 5'-ATGGCAGAGTGAGGGTTACCA-3'
Smdt1, Forward Primer 5'-ATTTTGCCCAAGCCGGTGAA-3'
Reverse Primer 5'-CCTCAAGCAGAGCAGCGAAG-3'
Micu1, Forward Primer 5'-CTTAACACCCTTTCTGCGTTGG-3'

Reverse Primer 5′-AGCATCAATCTTCGTTTGGTCT-3′
Micu2, Forward Primer 5′-CTCCGCAAACAGCGGTTCAT-3′
Reverse Primer 5′-TGCCAGCTTCTTGACCAGTG-3′
Micu3, Forward Primer 5′-GTAAGGTCAGAGCACGCAGAA-3′
Reverse Primer 5′-TTTCCTGTTGGACGCTGACAA −3′

cDNA (100 ng, calculated from initial RNA) samples were pre-amplified for 12 cycles using ABsolute qPCR SYBR Green Low ROX Mix (ThermoFisher). qPCR reactions were performed using an Agilent MX3000 (Fluidigm) with 40 cycles of amplification (15 s at 95˚C, 5 s at 70˚C, and 60 s at 60˚C). Ct values were calculated by the Real-Time PCR Analysis Software (Fluidigm). Relative gene expression was determined by the ΔCt method. *Hprt* was selected as the reference gene.

Generation of knockout cell lines by the CRISPR/Cas9 method

Knockout MEF cell lines were generated using the CRISPR/Cas9 method (***Ran et al., 2013***). All knockouts (except the MCU-KO line) were generated by Alstem LLC (Richmond, CA, USA). Either one sgRNA or a pair of two adjacent sgRNAs were used to create a point indel or a truncate indel, respectively (Figure S1).

Mcu, TGGCAGCGCTCGCGTCGAGA GGG
Smdt1, GAGTGTCCCGACATAGAGAA AGG
CTTACACTCCCACTAGGTTA AGG
Micu1, TCACTTTTAGATGCTGCCGG TGG
CTGCAAGTACCGGTCTCCTG TGG
Micu2, CGTTCGGGAGCCCTCGCGCG CGG
GGGCGCTTCCGCAAAGATGG CGG
Micu3, GGGCGAGCTGAGCATCGCGG CGG
CCGGGGCCGCTAGCTCCGAG GGG

MEFs were transfected with the Cas9 gRNA vector (Addgene: PX459) via electroporation (Invitrogen Neon transfection system) using the following parameters: 1×10^6 cells and 1 µg of two different gRNA-Cas9 plasmids. Puromycin was used for enrichment of transfected cells, and serial dilution was performed to select single-cell clones. A stable homozygous knockout cell line was confirmed by PCR amplification of the targeted region, cloning into a pUC19 vector, and sequencing showing that either a frameshift or large deletion had occurred in the targeted region of the gene (***Figure 1—figure supplement 1***). All knockout clones were further validated by western blotting (***Figure 1—figure supplement 1***). The primers used for amplification of genomic sites and cloning into pUC19 sequencing vector were as follows:

Mcu, Forward Primer TAGAAGCTTTCCACTGCTCTGATTGATCTTG
Reverse Primer ATGTGAATTCGAGCTGCTTTGGAATGAGAC
Smdt1, Forward Primer GTGAAGCTTGGGATCAGTAGTCCATTGGAGG
Reverse Primer AGGAGAATTCAGTGAGAGTTCCTGTGGTATG
Micu1, Forward Primer TTTAAGCTTGATTCCTTTGAGTTATAAGTAG
Reverse Primer CAAAGAATTCAGCAAAGAAATTCTGATGTA
Micu2, Forward Primer ACCAAGCTTGAACGTCGAGGAAGCAGCCAC
Reverse Primer AGGAGAATTCTCCATCCACCAGGTGGGCAG
Micu3, Forward Primer CGCAAGCTTCTCGCGAGATTTCGGCCCGCC
Reverse Primer AGGAGAATTCTCCATCCACCAGGTGGGCAG

Isolation of mitochondria and mitoplasts

Mitoplasts were isolated from MEFs using methodology previously described (***Garg and Kirichok, 2019***). Briefly, MEFs were homogenized in ice-cold medium (Initial medium) containing 250 mM sucrose, 10 mM HEPES, 1 mM EGTA, and 0.1% bovine serum albumin (BSA) (pH adjusted to 7.2 with Trizma base) using a glass grinder with six slow strokes of a Teflon pestle rotating at 280 rpm. The homogenate was centrifuged at 700× g for 10 min to create a pellet of nuclei and unbroken cells. The first nuclear pellet was resuspended in the fresh Initial medium and homogenized again to increase the mitochondrial yield. Mitochondria were collected by centrifugation of the supernatant at 8500× g for 10 min.

Mitoplasts were produced from mitochondria using a French press. Mitochondria were suspended in a hypertonic solution containing 140 mM sucrose, 440 mM D-mannitol, 5 mM HEPES, and 1 mM EGTA (pH adjusted to 7.2 with Trizma base) and then subjected to a French press at 1200–2000 psi to rupture the outer membrane. Mitoplasts were pelleted at 10,500× g for 15 min and resuspended for storage in 0.5–1 ml of solution containing 750 mM KCl, 100 mM HEPES, and 1 mM EGTA (pH adjusted to 7.2 with Trizma base). Mitoplasts prepared and stored with this method contained the same amount of auxiliary MICU1 and MICU2 subunits as compared to intact mitochondria (***Figure 1—figure supplement 2F***, see TCo-immunoprecipitation section below).

Mitochondria and mitoplasts were prepared at 0–4˚C and stored on ice for up to 5 hr. Immediately before the electrophysiological experiments, 15–50 µl of the mitoplast suspension was added to 500 µl solution containing 150 mM KCl, 10 mM HEPES, and 1 mM EGTA (pH adjusted to 7.0 with Trizma base) plating on 5 mm coverslips pretreated with 0.1% gelatin to reduce mitoplast adhesion.

Patch-clamp recording

Whole mitoplast currents were measured as described previously (***Garg and Kirichok, 2019***). Gigaohm seals with mitoplasts were formed in the bath solution containing 150 mM KCl, 10 mM HEPES and 1 mM EGTA, pH 7.2 (adjusted with KOH). Voltage steps of 350–500 mV for 2–8 ms were applied to rupture the IMM and obtain the whole-mitoplast conFiguration. Typically, pipettes had resistances of 20–40 MΩ, and the access resistance was 35–65 MΩ. The membrane capacitances of mitoplasts range from 0.2 to 0.6 pF.

All indicated voltages are on the matrix side of the IMM (pipette solution), relative to the cytosolic side (bath solution, ***Figure 1—figure supplement 2D***; ***Figure 1—figure supplement 2E***; ***Garg and Kirichok, 2019***). Currents were normally induced by a voltage ramp from −160 mV to +80 mV (interval between pulses was 5 s) to cover all physiological voltages across the IMM, but other voltage protocols were also used as indicated in the Figures. All whole-IMM recordings were performed under continuous perfusion of the bath solution. Currents were normalized per membrane capacitance to obtain current densities (pA/pF). Currents flowing into mitochondria are shown as negative, while those flowing out are positive. Membrane capacitance transients *observed* upon application of voltage steps were removed from current traces.

Typically, pipettes were filled with one of the following three solutions (***Garg and Kirichok, 2019***) (tonicity was adjusted to ~350 mmol/kg with sucrose).

Solution A was used to measure Ca^{2+} currents and contained: 110 mM Na-gluconate, 40 mM HEPES, 10 mM EGTA and 2 mM $MgCl_2$ (pH 7.0 with NaOH).

Solution B was used to measure Na^+ or Mn^{2+} currents and contained: 110 Na-gluconate, 40 HEPES, 1 EGTA, 5 EDTA, and 2 mM NaCl (pH 7.0 with Tris base).

Solution C was used to measure outward Ca^{2+} currents (the MCU rectification experiments) and contained: 130 mM tetramethylammonium hydroxide (TMA), 100 mM HEPES and 2 mM $CaCl_2$ (pH 7.0 with D-gluconic acid).

To measure whole-mitoplast Ca^{2+} currents, the bath solution was formulated to contain only 150 mM HEPES (pH 7.0 with Tris base, tonicity ~300 mmol/kg with sucrose) and different dilutions of $CaCl_2$ from a 1 M stock (Sigma) (***Kirichok et al., 2004***). The control solution contained: 150 mM HEPES, 80 mM sucrose and 1 mM EGTA (pH 7.0 with Tris base, tonicity ~300 mmol/kg with sucrose). The bath solution used for measuring Na^+ current contained: 110 mM Na-gluconate, 40 mM HEPES, 1 mM EGTA and 5 mM EDTA (pH 7.0 with Tris base, tonicity ~300 mmol/kg with sucrose). The bath solution for measuring inhibition of Na^+ current by cytosolic Ca^{2+} contained: 110 mM Na-gluconate, 40 mM HEPES, and 10 mM EDTA (pH 8.0 with Tris, tonicity ~380 mmol/kg with sucrose) and varying amounts of $CaCl_2$ were added to the bath solution to achieve the free [Ca^{2+}] calculated using the MaxChelator program (C. Patton, Stanford University).

A rapid exchange of $[Ca^{2+}]_i$ from virtual zero (control solution) to 1 mM was achieved using a commercially available fast solution exchange system (Warner Instruments, SF-77B perfusion fast step system). It was interfaced with our pClamp acquisition software in order to precisely time the steps during solution change. The timing (τ ~0.4 ms) for solution exchange was judged by the current changes because of a junction potential difference using solutions with different ionic strengths.

Currents were recorded using an Axopatch 200B amplifier (Molecular Devices). Data acquisition and analyses were performed using PClamp 10 (Molecular Devices) and Origin 9.6 (OriginLab). All data were acquired at 10 kHz and filtered at 1 kHz.

Single-channel recordings and analysis

All single-channel data were acquired from inside–out patches excised from isolated mitoplasts (**Kirichok et al., 2004**). For Ca^{2+} single channel (i_{Ca}) recordings, patches were excised in a bath solution containing 150 mM KCl, 10 mM HEPES and 1 mM EGTA, pH 7.2 (adjusted with KOH). Recordings were performed under symmetrical conditions (the same bath and pipette solutions): 105 mM $CaCl_2$ and 40 mM HEPES, pH 7.0 with Tris base. Signals were sampled at 50 kHz and low-pass filtered at 1 kHz. Fire-polished, borosilicate pipettes (Sutter QF-150–75) coated with Silguard (Dow Corning Corp., Midland, MI) and having a tip resistance of 50–70 MΩ were used for low noise recordings.

For Na^+ single channel (i_{Na}) recordings, patches were excised in a bath solution containing 150 mM Na-gluconate, 10 mM HEPES, 1 mM EGTA and 1 mM $MgCl_2$, pH 7.2 (adjusted with NaOH). Pipette solution contained 150 mM Na-gluconate, 10 mM HEPES, 1 mM EGTA, 1 mM EDTA, and 2 mM NaCl, pH 7.2 (adjusted with NaOH). Signals were sampled at 50 kHz and low-pass filtered at 1 kHz.

To characterize the single-channel conductance and subconductance levels and their occupancy probabilities, we used the MLab version of the QuB software, freely available from the Milescu lab at: https://milesculabs.biology.missouri.edu/QuB_Downloads.html. The data were first resampled at 2.5 kHz and then were idealized with the Baum-Welch and Viterbi algorithms, as implemented in QuB, which classify each point in the data to a conductance level and produce estimates of current amplitudes and occupancy probabilities. The time-averaged single-channel current can be calculated as the product between occupancy probability and current amplitude, summated over all conductance levels (main open state and substates).

Time-lapse Ca^{2+} imaging in intact cells

For imaging experiments, MEFs were plated on collagen type-I-coated glass-bottom 35 mm dishes (P35G-1.5–14 C, Matek), 48–72 hr before imaging. Cells were imaged at the interval of 3 s on a Nikon Ti-E microscope using a 40× objective (NA 1.30, oil, CFI Plan Fluor, Nikon), Lambda 421 LED light source (Sutter) and ORCA Flash 4.0 CMOS camera (Hamamatsu Photonics) at room temperature (25˚C). The following excitation/emission filter settings were used: 340±13/525±25 nm and 389±19/510±40 nm for cytosolic Ca^{2+} imaging using fura-2 (K_d=224 nM) and 480±40/525±15 nm for mitochondrially targeted *cepia2* (*CEPIA2mt*, K_d=160 nM (**Suzuki et al., 2014**), cloned into a lentiviral vector). Cells were loaded with 3 µM fura-2 AM (Life Tech., USA) in DMEM/FBS at room temperature for 30 min. After three washes with physiological salt solution (PSS) containing (in mM) 150 NaCl, 4 KCl, 2 $CaCl_2$, 1 $MgCl_2$, 5.6 glucose, and 25 HEPES (pH 7.4), each dish was placed on the stage for imaging. Imaging was performed in PSS within 1 hr of dye staining. Baseline fluorescence was taken for 1–2 min after which thapsigargin (Tg) (final [Tg] = 300 nM) was added while imaging was continued for another 10–15 min.

Fura-2 calibration

Baseline measurements were taken, and cells were incubated in PSS (No $CaCl_2$) containing 3 mM EGTA, 1 µM ionomycin and 1 µM Tg for 5–10 min. After 2–3 washes with PSS (No $CaCl_2$) containing 0.3 mM EGTA, cells were imaged for 5 min (average of last 10 frames was used for calculation) to obtain the R_{min} and F_{380max} values. Finally, PSS containing 10 mM $CaCl_2$ (no EGTA), 1 µM ionomycin and 1 µM Tg was added and cells were imaged for 10 min. After the signal reached saturation (~3 min), the average value from 10 frames was used to calculate R_{max} and F_{380min} values. Using these obtained values, the fura-2 ratio was calibrated by the following equation (**Grynkiewicz et al., 1985**):

$$[Ca^{2+}]_{free} = K_d * \left(\frac{[R - R_{min}]}{[R_{max}]}\right) * (F_{380max}/F_{380min})$$

All image analyses were done with ImageJ (NIH). Briefly, mitochondrial and cytosolic regions were manually determined for each cell. The average fluorescence intensity in the regions was measured and the background intensity was subtracted. For analysis of the *cepia2* signal, we normalized the fluorescence intensity by the baseline fluorescence. For analysis of the fura-2 signal, we calculated the fluorescence ratio (F_{340}/F_{380} for fura-2).

The time point for increase in mitochondrial [Ca^{2+}] (upstroke) was detected using a script written in Python and manually checked afterwards. Briefly, the fluorescence signal was smoothed by applying a second-order zero phase digital Butterworth filter with an optimal cutoff frequency as previously described (**Winter, 2009**). From the smoothed signal, the upstroke frame was defined as the earliest point between the baseline and signal peak that was greater than 80% of the maximal time derivative. The time-point for change in mitochondrial signal was time-matched with the fura-2 reading to determine the threshold $[Ca^{2+}]_i$.

Measurements of mitochondrial Ca^{2+} influx in isolated mitochondria

Briefly, mitochondria were isolated from MEF cells using differential centrifugation as described above. The mitochondrial pellet was resuspended in resuspension buffer (RB) supplemented with 2 mM EGTA and 2 µM of Fura-2-acetoxymethyl ester (Fura-2 AM) and kept at room temperature for 10 min to allow loading of Fura-2 into the mitochondrial matrix. The RB buffer contained: 100 mM KCl, 50 mM MOPS, 1 mM $MgCl_2$. Mitochondria were pelleted at 3200 g, and further incubated on ice for 50 min to allow de-esterification of Fura-2 AM in RB supplemented with 2 mM EGTA. Mitochondria were pelleted at 3200 g and resuspended in RB supplemented with 10 µM EGTA. Mitochondria were further pelleted and resuspended twice in RB supplemented with 40 µM Fluo-4 pentapotassium salt (for measurements carried out below 3 µM $[Ca^{2+}]_i$), or RB supplemented with 40 µM EGTA (for measurements carried out above 3 µM $[Ca^{2+}]_i$). After final centrifugation step at 3200 g, protein concentration was determined by Lowry assay.

Measurements of mitochondrial Ca^{2+} influx were carried out using a BMG LABTECH CLARIOstar plate reader as described before (**Wescott et al., 2019**). Experiments were carried out with mitochondria (0.5 mg/ml) in an uptake assay buffer (uAB) that contained: 130 mM KCl, 20 mM HEPES, 1 mM $MgCl_2$, 1 mM K_2HPO_4, pH 7.2 (with KOH), supplemented with energetic substrates (glutamate, malate and succinate, each 5 mM), and 1 µM TMRM. The uAB and all the stock solutions were made with analytical-grade deionized water (OmniSolv LC–MS, Sigma Aldrich) and contained less than 50 nM of residual [Ca^{2+}] (measured daily). After 3 min of incubation with substrates, assays were initiated by injection of 100 µl of Ca^{2+} stock to bring the final volume to 200 µl. TMRM (ex: 546 ± 4 nm and 573 ± 5 nm, em: 619 ± 15 nm) and Fura-2 (ex: 335 ± 6 nm and 380 ± 6 nm, em: 490 ± 15 nm) fluorescence were measured, along with Fluo-4 or Fluo4-FF (ex: 485 nm, em: 520–542 nm) within the same well for 35 s. To measure MCU Ca^{2+} flux (J_{MCU}), two protocols were used. Protocol 1 ([Ca^{2+}] range $\leq$ 3 µM): here, Fluo-4 (3 µM) is the single significant buffer of extra-mitochondrial Ca^{2+} (i.e., $[Ca^{2+}]_i$). Protocol 2 ([Ca^{2+}] range from 4 µM to 25 µM): here mitochondria were suspended in 40 µM EGTA and 1 µM Fluo4-FF was used. Total Ca^{2+} influx (J) is taken as the first derivative of the linear fit to the measured total extramitochondrial [Ca^{2+}] over the first 20 s of each experiment. The total Ca^{2+} conductance of the IMM (G) was obtained from the simultaneous measurements of J, $[Ca^{2+}]_i$, $[Ca^{2+}]_m$ and $\Delta\Psi_m$ according to the typical Hodgkin–Huxley model (**Wescott et al., 2019**):

$I = G\ (\Delta\Psi_m - E_{Ca}^{2+})$ where E_{Ca}^{2+} is the Nernst reversal potential for Ca^{2+} obtained from simultaneously measured $[Ca^{2+}]_i$, and $[Ca^{2+}]_m$. Measured J was converted to I using the Faraday constant (**Wescott et al., 2019**).

Measurements of mitochondrial Na^+ influx in isolated mitochondria

Membrane potentials in intact mitochondria were evaluated with TMRE using previously described method (**Scaduto and Grotyohann, 1999**). Mitochondria isolated from mouse liver or MEF cells were suspended in ice-cold initial medium. These mitochondria were mixed in 50–100 µl of an uptake assay buffer (liver: 150 mM NaCl, 10 mM HEPES, 1 mM EGTA, 2 mM glutamate, 2 mM malate, and 2 mM succinate, pH 7.2 with Trizma base; MEF: 30 mM NaCl, 120 mM TrisCl, 10 mM HEPES, 1 mM EGTA, 1 µM $MgCl_2$, 5 mM glutamate, 5 mM malate, and 5 mM succinate, pH 7.2 with Trizma base) with 200 nM TMRE. Mitochondrial concentration in the assay buffer was 0.25 mg/ml. TMRE fluorescence were measured at 550/570 nm and 570/589 nm (excitation/emission, 9 nm band width) with using a Biotek Synergy H4 plate reader, and the fluorescence ratio between two fluorescence was calculated. After 5 min incubation of mitochondria in the assay medium, assays were initiated by injection of 0.5–1 µl of EDTA (5 mM final), RuR (1–3 µM final) or FCCP (1 µM final), and the ratio change within 5 min after the injection was evaluated. The ratio change induced by EDTA and/or RuR was normalized with that by FCCP.

Co-immunoprecipitation

Mitochondria or mitoplasts were isolated from MEFs deficient in the MCU subunit but stably expressing Flag-tagged MCU. Mitochondrial fraction from wild type cells (without MCU-FLAG) was used as negative control. Isolated mitoplasts (but not mitochondria) were incubated in 750 mM KCl for 30 min before solubilization. Briefly, 300 µg of protein lysate was solubilized with 500 µl of lysis buffer (50 mM HEPES pH 7.4, 150 mM NaCl, 1 mM EGTA, 0.2% DDM and Halt protease inhibitor cocktail [Thermo Fisher]) for 30 min at 4˚C. Lysates were cleared by spinning at 20,000× g for 10 min at 4˚C. Cleared lysates were incubated with anti-Flag M2 affinity gel (Sigma A2220) for 2 hr at 4˚C. Immunoprecipitates were washed with 1 ml of lysis buffer three times and boiled in 20 µl of Laemmli buffer (without β-mercaptoethanol). One-third of the immunoprecipitate was loaded onto a 4–20% gradient SDS-PAGE gel for detection of the indicated proteins by Western blotting. Flow-through fraction was also collected and analyzed in the same gel.

Immunoblots

For western blot analysis, MEFs or isolated mitochondria/mitoplasts were lysed in radioimmunoprecipitation assay (RIPA) buffer (1% IGEPAL, 0.1% sodium dodecyl sulfate, 0.5% sodium deoxycholate, 150 mM NaCl, 1 mM EDTA, 50 mM Tris-HCl (pH 7.4) and a cocktail of proteases inhibitors). Lysates were resolved by SDS-PAGE; transferred to PVDF membrane (Millipore); and probed with anti-MCU (Sigma, HPA016480, 1:2000), anti-EMRE (Santa Cruz, sc-86337, 1:200), anti-HSP60 (Santa Cruz, sc-1052, 1:3000), anti-VDAC (Abcam, ab15895, 1:2000), anti-MICU1 (Cell Signaling Technology, 12524S, 1:2000), anti-MICU2 (Bethyl, A300-BL19212, 1:500), anti-MICU3 (Sigma, HPA024779, 1:1000), and anti-TOM20 (Santa Cruz, sc-11415, 1:2000). Anti-MICU1 antibody produced a non-specific band near its monomeric molecular weight (~50 kDa), so samples were prepared in Laemmli buffer without β-mercaptoethanol to detect MICU1 homo- or heterodimers (~100 kDa).

Statistical analysis

Data are presented as mean ± standard error of the mean (SEM), as specified in the Figure legend. Statistical analysis was completed in Excel or Origin 9.6. All experiments were performed in triplicate or more. Statistical significance at an exact p-*value* was determined with the methods as indicated in the corresponding Figure legends.

Acknowledgements

We thank Drs. Katsuyoshi Mihara (Kyushu University, Japan) and David C. Chan (Caltech, USA) for sending us DRP1-KO MEFs, and Dr. Toren Finkel (University of Pittsburgh, USA) for sending the MEFs with intact DRP1 (WT and MICU1-KO MEFs) and the MCU-KO mice. We thank the Nikon Microscopy Core (DeLaine Larsen, Kari Herrington) and Lab for Cell Analysis (Sarah Elms) at UCSF for help with use of microscopy and FACS equipment. We thank all members of the YK lab for helpful discussions. This work was supported by American Heart Association Scientist Development Grant 17SDG33660926 (VG) and NIH grant 5R01GM107710 (YK) and R35GM136415 (YK).

Additional information

Funding

Funder	Grant reference number	Author
National Institutes of Health	R01GM134536	Yuriy Kirichok
National Institutes of Health	R35GM136415	Yuriy Kirichok
American Heart Association	17SDG33660926	Vivek Garg

The funders had no role in study design, data collection and interpretation, or the decision to submit the work for publication.

Author contributions

Vivek Garg, Conceptualization, Resources, Software, Formal analysis, Supervision, Funding acquisition, Validation, Investigation, Visualization, Methodology, Writing - original draft, Project administration, Writing - review and editing; Junji Suzuki, Formal analysis, Investigation, Visualization, Methodology; Ishan Paranjpe, Software, Investigation; Tiffany Unsulangi, Investigation; Liron Boyman, Investigation, Methodology, Writing - review and editing; Lorin S Milescu, Software- Formal analysis; W Jonathan Lederer, Resources, Supervision, Methodology, Writing - review and editing; Yuriy Kirichok, Conceptualization, Resources, Data curation, Supervision, Funding acquisition, Methodology, Writing - original draft, Project administration, Writing - review and editing

Author ORCIDs

Vivek Garg https://orcid.org/0000-0002-6940-5415
Yuriy Kirichok https://orcid.org/0000-0001-7155-843X

Ethics

Animal experimentation: All animal experiments were performed according to procedures approved by the UCSF Institutional Animal Care and Use Committee (approval # AN183460-02A) and adhered to NIH standards.

Decision letter and Author response

Decision letter https://doi.org/10.7554/eLife.69312.sa1
Author response https://doi.org/10.7554/eLife.69312.sa2

Additional files

Supplementary files

- Supplementary file 1. MICU1 effect on MCU_{cx}. (a) MICU1 effect on MCU_{cx} as determined by previous electrophysiological experiments. (b) MICU1 effect on MCU_{cx} as determined by previous Ca^{2+} imaging experiments.
- Transparent reporting form

Data availability

Due to the size of the dataset, raw electrophysiology traces are available on request to the corresponding author. All information has been extracted from the raw electrophysiological traces and is available to download as source data files. All the codes or software used in analyzing the data and their sources are listed in the Key Resources Table.

References

Allshire A, Bernardi P, Saris NE. 1985. Manganese stimulates calcium flux through the mitochondrial uniporter. *Biochimica Et Biophysica Acta (BBA) - Bioenergetics* **807**:202–209. DOI: https://doi.org/10.1016/0005-2728(85)90123-9, PMID: 3978095

Ashrafi G, de Juan-Sanz J, Farrell RJ, Ryan TA. 2020. Molecular tuning of the axonal mitochondrial Ca^{2+} uniporter ensures metabolic flexibility of neurotransmission. *Neuron* **105**:678–687. DOI: https://doi.org/10.1016/j.neuron.2019.11.020, PMID: 31862210

Baradaran R, Wang C, Siliciano AF, Long SB. 2018. Cryo-EM structures of fungal and metazoan mitochondrial calcium uniporters. *Nature* **559**:580–584. DOI: https://doi.org/10.1038/s41586-018-0331-8, PMID: 29995857

Baughman JM, Perocchi F, Girgis HS, Plovanich M, Belcher-Timme CA, Sancak Y, Bao XR, Strittmatter L, Goldberger O, Bogorad RL, Koteliansky V, Mootha VK. 2011. Integrative genomics identifies MCU as an essential component of the mitochondrial calcium uniporter. *Nature* **476**:341–345. DOI: https://doi.org/10.1038/nature10234, PMID: 21685886

Bernardi P. 1999. Mitochondrial transport of cations: channels, exchangers, and permeability transition. *Physiological Reviews* **79**:1127–1155. DOI: https://doi.org/10.1152/physrev.1999.79.4.1127, PMID: 10508231

Berridge MJ, Bootman MD, Roderick HL. 2003. Calcium signalling: dynamics, homeostasis and remodelling. *Nature Reviews. Molecular Cell Biology* **4**:517–529. DOI: https://doi.org/10.1038/nrm1155, PMID: 12838335

Bertolini MS, Chiurillo MA, Lander N, Vercesi AE, Docampo R. 2019. MICU1 and MICU2 play an essential role in mitochondrial Ca^{2+} uptake, growth, and infectivity of the human pathogen Trypanosoma cruzi. *mBio* **10**: e00348-19. DOI: https://doi.org/10.1128/mBio.00348-19, PMID: 31064825

Boyman L, Williams GS, Khananshvili D, Sekler I, Lederer WJ. 2013. NCLX: the mitochondrial sodium calcium exchanger. *Journal of Molecular and Cellular Cardiology* **59**:205–213. DOI: https://doi.org/10.1016/j.yjmcc.2013.03.012, PMID: 23538132

Chaudhuri D, Sancak Y, Mootha VK, Clapham DE. 2013. MCU encodes the pore conducting mitochondrial calcium currents. *eLife* **2**:e00704. DOI: https://doi.org/10.7554/eLife.00704, PMID: 23755363

Colegrove SL, Albrecht MA, Friel DD. 2000a. Dissection of mitochondrial Ca^{2+} uptake and release fluxes in situ after depolarization-evoked $[Ca^{2+}]_i$ elevations in sympathetic neurons. *The Journal of General Physiology* **115**: 351–370. DOI: https://doi.org/10.1085/jgp.115.3.351, PMID: 10694263

Colegrove SL, Albrecht MA, Friel DD. 2000b. Quantitative analysis of mitochondrial Ca^{2+} uptake and release pathways in sympathetic neurons: reconstruction of the recovery after depolarization-evoked $[Ca^{2+}]_i$ elevations. *The Journal of General Physiology* **115**:371–388. DOI: https://doi.org/10.1085/jgp.115.3.371, PMID: 10694264

Csordás G, Golenár T, Seifert EL, Kamer KJ, Sancak Y, Perocchi F, Moffat C, Weaver D, Perez SF, Bogorad R, Koteliansky V, Adijanto J, Mootha VK, Hajnóczky G. 2013. MICU1 controls both the threshold and cooperative activation of the mitochondrial Ca^{2+} uniporter. *Cell Metabolism* **17**:976–987. DOI: https://doi.org/10.1016/j.cmet.2013.04.020, PMID: 23747253

De Stefani D, Raffaello A, Teardo E, Szabò I, Rizzuto R. 2011. A forty-kilodalton protein of the inner membrane is the mitochondrial calcium uniporter. *Nature* **476**:336–340. DOI: https://doi.org/10.1038/nature10230, PMID: 21685888

Deluca HF, Engstrom GW. 1961. Calcium uptake by rat kidney mitochondria. *PNAS* **47**:1744–1750. DOI: https://doi.org/10.1073/pnas.47.11.1744, PMID: 13885269

Dreolini L, Cullen M, Yung E, Laird L, Webb JR, Nelson BH, Hay KA, Balasundaram M, Kekre N, Holt RA. 2020. A rapid and sensitive Nucleic Acid Amplification Technique for *Mycoplasma* screening of cell therapy products. *Molecular Therapy. Methods & Clinical Development* **17**:393–399. DOI: https://doi.org/10.1016/j.omtm.2020.01.009, PMID: 32128343

Faas GC, Raghavachari S, Lisman JE, Mody I. 2011. Calmodulin as a direct detector of Ca^{2+} signals. *Nature Neuroscience* **14**:301–304. DOI: https://doi.org/10.1038/nn.2746, PMID: 21258328

Fan C, Fan M, Orlando BJ, Fastman NM, Zhang J, Xu Y, Chambers MG, Xu X, Perry K, Liao M, Feng L. 2018. X-ray and cryo-EM structures of the mitochondrial calcium uniporter. *Nature* **559**:575–579. DOI: https://doi.org/10.1038/s41586-018-0330-9, PMID: 29995856

Fan M, Zhang J, Tsai CW, Orlando BJ, Rodriguez M, Xu Y, Liao M, Tsai MF, Feng L. 2020. Structure and mechanism of the mitochondrial Ca^{2+} uniporter holocomplex. *Nature* **582**:129–133. DOI: https://doi.org/10.1038/s41586-020-2309-6, PMID: 32494073

Fieni F, Lee SB, Jan YN, Kirichok Y. 2012. Activity of the mitochondrial calcium uniporter varies greatly between tissues. *Nature Communications* **3**:1317. DOI: https://doi.org/10.1038/ncomms2325, PMID: 23271651

Foskett JK, Madesh M. 2014. Regulation of the mitochondrial Ca^{2+} uniporter by MICU1 and MICU2. *Biochemical and Biophysical Research Communications* **449**:377–383. DOI: https://doi.org/10.1016/j.bbrc.2014.04.146, PMID: 24792178

Garg V, Kirichok YY. 2019. Patch-Clamp Analysis of the Mitochondrial Calcium Uniporter. *Methods in Molecular Biology* **1925**:75–86. DOI: https://doi.org/10.1007/978-1-4939-9018-4_7, PMID: 30674018

Ghosh S, Basu Ball W, Madaris TR, Srikantan S, Madesh M, Mootha VK, Gohil VM. 2020. An essential role for cardiolipin in the stability and function of the mitochondrial calcium uniporter. *PNAS* **117**:16383–16390. DOI: https://doi.org/10.1073/pnas.2000640117, PMID: 32601238

Glancy B, Balaban RS. 2012. Role of mitochondrial Ca^{2+} in the regulation of cellular energetics. *Biochemistry* **51**: 2959–2973. DOI: https://doi.org/10.1021/bi2018909, PMID: 22443365

Gottschalk B, Klec C, Leitinger G, Bernhart E, Rost R, Bischof H, Madreiter-Sokolowski CT, Radulović S, Eroglu E, Sattler W, Waldeck-Weiermair M, Malli R, Graier WF. 2019. MICU1 controls cristae junction and spatially anchors mitochondrial Ca^{2+} uniporter complex. *Nature Communications* **10**:3732. DOI: https://doi.org/10.1038/s41467-019-11692-x, PMID: 31427612

Grynkiewicz G, Poenie M, Tsien RY. 1985. A new generation of Ca^{2+} indicators with greatly improved fluorescence properties. *The Journal of Biological Chemistry* **260**:3440–3450. PMID: 3838314

Gunter TE, Gerstner B, Lester T, Wojtovich AP, Malecki J, Swarts SG, Brookes PS, Gavin CE, Gunter KK. 2010. An analysis of the effects of Mn^{2+} on oxidative phosphorylation in liver, brain, and heart mitochondria using state 3 oxidation rate assays. *Toxicology and Applied Pharmacology* **249**:65–75. DOI: https://doi.org/10.1016/j.taap.2010.08.018, PMID: 20800605

Gunter TE, Pfeiffer DR. 1990. Mechanisms by which mitochondria transport calcium. *The American Journal of Physiology* **258**:C755–C786. DOI: https://doi.org/10.1152/ajpcell.1990.258.5.C755, PMID: 2185657

Hess P, Lansman JB, Tsien RW. 1986. Calcium channel selectivity for divalent and monovalent cations. Voltage and concentration dependence of single channel current in ventricular heart cells. *The Journal of General Physiology* **88**:293–319. DOI: https://doi.org/10.1085/jgp.88.3.293, PMID: 2428919

Hess P, Tsien RW. 1984. Mechanism of ion permeation through calcium channels. *Nature* **309**:453–456. DOI: https://doi.org/10.1038/309453a0, PMID: 6328315

Hoffman NE, Chandramoorthy HC, Shamugapriya S, Zhang X, Rajan S, Mallilankaraman K, Gandhirajan RK, Vagnozzi RJ, Ferrer LM, Sreekrishnanilayam K, Natarajaseenivasan K, Vallem S, Force T, Choi ET, Cheung JY,

Madesh M. 2013. MICU1 motifs define mitochondrial calcium uniporter binding and activity. *Cell Reports* **5**: 1576–1588. DOI: https://doi.org/10.1016/j.celrep.2013.11.026, PMID: 24332854

Holmström KM, Pan X, Liu JC, Menazza S, Liu J, Nguyen TT, Pan H, Parks RJ, Anderson S, Noguchi A, Springer D, Murphy E, Finkel T. 2015. Assessment of cardiac function in mice lacking the mitochondrial calcium uniporter. *Journal of Molecular and Cellular Cardiology* **85**:178–182. DOI: https://doi.org/10.1016/j.yjmcc.2015.05.022, PMID: 26057074

Hughes BP, Exton JH. 1983. Effect of micromolar concentrations of manganese ions on calcium-ion cycling in rat liver mitochondria. *The Biochemical Journal* **212**:773–782. DOI: https://doi.org/10.1042/bj2120773, PMID: 6192809

Hutson SM, Pfeiffer DR, Lardy HA. 1976. Effect of cations and anions on the steady state kinetics of energy-dependent Ca^{2+} transport in rat liver mitochondria. *The Journal of Biological Chemistry* **251**:5251–5258. PMID: 783158

Ishihara N, Nomura M, Jofuku A, Kato H, Suzuki SO, Masuda K, Otera H, Nakanishi Y, Nonaka I, Goto Y, Taguchi N, Morinaga H, Maeda M, Takayanagi R, Yokota S, Mihara K. 2009. Mitochondrial fission factor Drp1 is essential for embryonic development and synapse formation in mice. *Nature Cell Biology* **11**:958–966. DOI: https://doi.org/10.1038/ncb1907, PMID: 19578372

Kamer KJ, Grabarek Z, Mootha VK. 2017. High-affinity cooperative Ca^{2+} binding by MICU1-MICU2 serves as an on-off switch for the uniporter. *EMBO Reports* **18**:1397–1411. DOI: https://doi.org/10.15252/embr.201643748, PMID: 28615291

Kamer KJ, Sancak Y, Fomina Y, Meisel JD, Chaudhuri D, Grabarek Z, Mootha VK. 2018. MICU1 imparts the mitochondrial uniporter with the ability to discriminate between Ca^{2+} and Mn^{2+}. *PNAS* **115**:E7960–E7969. DOI: https://doi.org/10.1073/pnas.1807811115, PMID: 30082385

Kamer KJ, Mootha VK. 2014. MICU1 and MICU2 play nonredundant roles in the regulation of the mitochondrial calcium uniporter. *EMBO Reports* **15**:299–307. DOI: https://doi.org/10.1002/embr.201337946, PMID: 24503055

Kirichok Y, Krapivinsky G, Clapham DE. 2004. The mitochondrial calcium uniporter is a highly selective ion channel. *Nature* **427**:360–364. DOI: https://doi.org/10.1038/nature02246, PMID: 14737170

Kröner H. 1986. Ca^{2+} ions, an allosteric activator of calcium uptake in rat liver mitochondria. *Archives of Biochemistry and Biophysics* **251**:525–535. DOI: https://doi.org/10.1016/0003-9861(86)90360-7, PMID: 3800383

Kwong JQ, Lu X, Correll RN, Schwanekamp JA, Vagnozzi RJ, Sargent MA, York AJ, Zhang J, Bers DM, Molkentin JD. 2015. The mitochondrial calcium uniporter selectively matches metabolic output to acute contractile stress in the heart. *Cell Reports* **12**:15–22. DOI: https://doi.org/10.1016/j.celrep.2015.06.002, PMID: 26119742

Lansman JB, Hess P, Tsien RW. 1986. Blockade of current through single calcium channels by Cd^{2+}, Mg^{2+}, and Ca^{2+}. Voltage and concentration dependence of calcium entry into the pore. *The Journal of General Physiology* **88**:321–347. DOI: https://doi.org/10.1085/jgp.88.3.321, PMID: 2428920

Liu JC, Liu J, Holmström KM, Menazza S, Parks RJ, Fergusson MM, Yu ZX, Springer DA, Halsey C, Liu C, Murphy E, Finkel T. 2016. MICU1 serves as a molecular gatekeeper to prevent in vivo mitochondrial calcium overload. *Cell Reports* **16**:1561–1573. DOI: https://doi.org/10.1016/j.celrep.2016.07.011, PMID: 27477272

Logan CV, Szabadkai G, Sharpe JA, Parry DA, Torelli S, Childs AM, Kriek M, Phadke R, Johnson CA, Roberts NY, Bonthron DT, Pysden KA, Whyte T, Munteanu I, Foley AR, Wheway G, Szymanska K, Natarajan S, Abdelhamed ZA, Morgan JE, et al. 2014. Loss-of-function mutations in MICU1 cause a brain and muscle disorder linked to primary alterations in mitochondrial calcium signaling. *Nature Genetics* **46**:188–193. DOI: https://doi.org/10.1038/ng.2851, PMID: 24336167

Luongo TS, Lambert JP, Yuan A, Zhang X, Gross P, Song J, Shanmughapriya S, Gao E, Jain M, Houser SR, Koch WJ, Cheung JY, Madesh M, Elrod JW. 2015. The mitochondrial calcium uniporter matches energetic supply with cardiac workload during stress and modulates permeability transition. *Cell Reports* **12**:23–34. DOI: https://doi.org/10.1016/j.celrep.2015.06.017, PMID: 26119731

Luongo TS, Lambert JP, Gross P, Nwokedi M, Lombardi AA, Shanmughapriya S, Carpenter AC, Kolmetzky D, Gao E, van Berlo JH, Tsai EJ, Molkentin JD, Chen X, Madesh M, Houser SR, Elrod JW. 2017. The mitochondrial Na^{+}/Ca^{2+} exchanger is essential for Ca^{2+} homeostasis and viability. *Nature* **545**:93–97. DOI: https://doi.org/10.1038/nature22082

Mallilankaraman K, Cárdenas C, Doonan PJ, Chandramoorthy HC, Irrinki KM, Golenár T, Csordás G, Madireddi P, Yang J, Müller M, Miller R, Kolesar JE, Molgó J, Kaufman B, Hajnóczky G, Foskett JK, Madesh M. 2012a. MCUR1 is an essential component of mitochondrial Ca^{2+} uptake that regulates cellular metabolism. *Nature Cell Biology* **14**:1336–1343. DOI: https://doi.org/10.1038/ncb2622, PMID: 23178883

Mallilankaraman K, Doonan P, Cárdenas C, Chandramoorthy HC, Müller M, Miller R, Hoffman NE, Gandhirajan RK, Molgó J, Birnbaum MJ, Rothberg BS, Mak DO, Foskett JK, Madesh M. 2012b. MICU1 is an essential gatekeeper for MCU-mediated mitochondrial Ca^{2+} uptake that regulates cell survival. *Cell* **151**:630–644. DOI: https://doi.org/10.1016/j.cell.2012.10.011, PMID: 23101630

McCormack JG, Halestrap AP, Denton RM. 1990. Role of calcium ions in regulation of mammalian intramitochondrial metabolism. *Physiological Reviews* **70**:391–425. DOI: https://doi.org/10.1152/physrev.1990.70.2.391, PMID: 2157230

McCormack JG, Denton RM. 1993. Mitochondrial Ca^{2+} transport and the role of intramitochondrial Ca^{2+} in the regulation of energy metabolism. *Developmental Neuroscience* **15**:165–173. DOI: https://doi.org/10.1159/000111332, PMID: 7805568

Nemani N, Shanmughapriya S, Madesh M. 2018. Molecular regulation of MCU: Implications in physiology and disease. *Cell Calcium* **74**:86–93. DOI: https://doi.org/10.1016/j.ceca.2018.06.006, PMID: 29980025

Nguyen NX, Armache JP, Lee C, Yang Y, Zeng W, Mootha VK, Cheng Y, Bai XC, Jiang Y. 2018. Cryo-EM structure of a fungal mitochondrial calcium uniporter. *Nature* **559**:570–574. DOI: https://doi.org/10.1038/s41586-018-0333-6, PMID: 29995855

Nicholls DG. 2005. Mitochondria and calcium signaling. *Cell Calcium* **38**:311–317. DOI: https://doi.org/10.1016/j.ceca.2005.06.011, PMID: 16087232

Palty R, Silverman WF, Hershfinkel M, Caporale T, Sensi SL, Parnis J, Nolte C, Fishman D, Shoshan-Barmatz V, Herrmann S, Khananshvili D, Sekler I. 2010. NCLX is an essential component of mitochondrial Na^+/Ca^{2+} exchange. *PNAS* **107**:436–441. DOI: https://doi.org/10.1073/pnas.0908099107, PMID: 20018762

Pan X, Liu J, Nguyen T, Liu C, Sun J, Teng Y, Fergusson MM, Rovira II, Allen M, Springer DA, Aponte AM, Gucek M, Balaban RS, Murphy E, Finkel T. 2013. The physiological role of mitochondrial calcium revealed by mice lacking the mitochondrial calcium uniporter. *Nature Cell Biology* **15**:1464–1472. DOI: https://doi.org/10.1038/ncb2868, PMID: 24212091

Paranjpe I, Garg V, Kirichok Y. 2019. upstroke. *GitHub*. a21ed00. https://github.com/ishanparanjpe/upstroke

Patron M, Checchetto V, Raffaello A, Teardo E, Vecellio Reane D, Mantoan M, Granatiero V, Szabò I, De Stefani D, Rizzuto R. 2014. MICU1 and MICU2 finely tune the mitochondrial Ca^{2+} uniporter by exerting opposite effects on MCU activity. *Molecular Cell* **53**:726–737. DOI: https://doi.org/10.1016/j.molcel.2014.01.013, PMID: 24560927

Patron M, Granatiero V, Espino J, Rizzuto R, De Stefani D. 2019. MICU3 is a tissue-specific enhancer of mitochondrial calcium uptake. *Cell Death and Differentiation* **26**:179–195. DOI: https://doi.org/10.1038/s41418-018-0113-8, PMID: 29725115

Perocchi F, Gohil VM, Girgis HS, Bao XR, McCombs JE, Palmer AE, Mootha VK. 2010. MICU1 encodes a mitochondrial EF hand protein required for Ca^{2+} uptake. *Nature* **467**:291–296. DOI: https://doi.org/10.1038/nature09358, PMID: 20693986

Petrungaro C, Zimmermann KM, Küttner V, Fischer M, Dengjel J, Bogeski I, Riemer J. 2015. The Ca^{2+}-dependent release of the Mia40-induced MICU1-MICU2 dimer from MCU regulates mitochondrial Ca^{2+} uptake. *Cell Metabolism* **22**:721–733. DOI: https://doi.org/10.1016/j.cmet.2015.08.019, PMID: 26387864

Plovanich M, Bogorad RL, Sancak Y, Kamer KJ, Strittmatter L, Li AA, Girgis HS, Kuchimanchi S, De Groot J, Speciner L, Taneja N, Oshea J, Koteliansky V, Mootha VK. 2013. MICU2, a paralog of MICU1, resides within the mitochondrial uniporter complex to regulate calcium handling. *PLOS ONE* **8**:e55785. DOI: https://doi.org/10.1371/journal.pone.0055785, PMID: 23409044

Ran FA, Hsu PD, Wright J, Agarwala V, Scott DA, Zhang F. 2013. Genome engineering using the CRISPR-Cas9 system. *Nature Protocols* **8**:2281–2308. DOI: https://doi.org/10.1038/nprot.2013.143, PMID: 24157548

Sancak Y, Markhard AL, Kitami T, Kovács-Bogdán E, Kamer KJ, Udeshi ND, Carr SA, Chaudhuri D, Clapham DE, Li AA, Calvo SE, Goldberger O, Mootha VK. 2013. EMRE is an essential component of the mitochondrial calcium uniporter complex. *Science* **342**:1379–1382. DOI: https://doi.org/10.1126/science.1242993, PMID: 24231807

Scaduto RC, Grotyohann LW. 1999. Measurement of mitochondrial membrane potential using fluorescent rhodamine derivatives. *Biophysical Journal* **76**:469–477. DOI: https://doi.org/10.1016/S0006-3495(99)77214-0, PMID: 9876159

Suzuki J, Kanemaru K, Ishii K, Ohkura M, Okubo Y, Iino M. 2014. Imaging intraorganellar Ca^{2+} at subcellular resolution using CEPIA. *Nature Communications* **5**:4153. DOI: https://doi.org/10.1038/ncomms5153, PMID: 24923787

Tang L, Gamal El-Din TM, Payandeh J, Martinez GQ, Heard TM, Scheuer T, Zheng N, Catterall WA. 2014. Structural basis for Ca^{2+} selectivity of a voltage-gated calcium channel. *Nature* **505**:56–61. DOI: https://doi.org/10.1038/nature12775, PMID: 24270805

Tomar D, Thomas M, Garbincius JF, Kolmetzky DW, Salik O, Jadiya P, Carpenter AC, Elrod JW. 2019. MICU1 regulates mitochondrial cristae structure and function independent of the mitochondrial calcium uniporter channel. *bioRxiv*. DOI: https://doi.org/10.1101/803213

Tufi R, Gleeson TP, von Stockum S, Hewitt VL, Lee JJ, Terriente-Felix A, Sanchez-Martinez A, Ziviani E, Whitworth AJ. 2019. Comprehensive genetic characterization of mitochondrial Ca^{2+} uniporter components reveals their different physiological requirements in vivo. *Cell Reports* **27**:1541–1550. DOI: https://doi.org/10.1016/j.celrep.2019.04.033, PMID: 31042479

Vais H, Mallilankaraman K, Mak DD, Hoff H, Payne R, Tanis JE, Foskett JK. 2016. EMRE Is a matrix Ca^{2+} sensor that governs gatekeeping of the mitochondrial Ca^{2+} uniporter. *Cell Reports* **14**:403–410. DOI: https://doi.org/10.1016/j.celrep.2015.12.054, PMID: 26774479

Vais H, Payne R, Paudel U, Li C, Foskett JK. 2020. Coupled transmembrane mechanisms control MCU-mediated mitochondrial Ca^{2+} uptake. *PNAS* **117**:21731–21739. DOI: https://doi.org/10.1073/pnas.2005976117, PMID: 32801213

Vinogradov A, Scarpa A. 1973. The initial velocities of calcium uptake by rat liver mitochondria. *The Journal of Biological Chemistry* **248**:5527–5531. PMID: 4768910

Wang Y, Nguyen NX, She J, Zeng W, Yang Y, Bai XC, Jiang Y. 2019. Structural mechanism of EMRE-dependent gating of the human mitochondrial calcium uniporter. *Cell* **177**:e1213. DOI: https://doi.org/10.1016/j.cell.2019.03.050, PMID: 31080062

Wang C, Jacewicz A, Delgado BD, Baradaran R, Long SB. 2020a. Structures reveal gatekeeping of the mitochondrial Ca^{2+} uniporter by MICU1-MICU2. *eLife* **9**:e59991. DOI: https://doi.org/10.7554/eLife.59991, PMID: 32667285

Wang Y, Han Y, She J, Nguyen NX, Mootha VK, Bai XC, Jiang Y. 2020b. Structural insights into the Ca^{2+}-dependent gating of the human mitochondrial calcium uniporter. *eLife* **9**:e60513. DOI: https://doi.org/10.7554/eLife.60513, PMID: 32762847

Wescott AP, Kao JPY, Lederer WJ, Boyman L. 2019. Voltage-energized calcium-sensitive ATP production by mitochondria. *Nature Metabolism* **1**:975–984. DOI: https://doi.org/10.1038/s42255-019-0126-8, PMID: 31950102

Wettmarshausen J, Goh V, Huang KT, Arduino DM, Tripathi U, Leimpek A, Cheng Y, Pittis AA, Gabaldón T, Mokranjac D, Hajnóczky G, Perocchi F. 2018. MICU1 confers protection from MCU-dependent manganese toxicity. *Cell Reports* **25**:1425–1435. DOI: https://doi.org/10.1016/j.celrep.2018.10.037, PMID: 30403999

Williams GS, Boyman L, Chikando AC, Khairallah RJ, Lederer WJ. 2013. Mitochondrial calcium uptake. *PNAS* **110**:10479–10486. DOI: https://doi.org/10.1073/pnas.1300410110, PMID: 23759742

Winter DA. 2009. *Biomechanics and Motor Control of Human Movement*. Hoboken: Wiley. DOI: https://doi.org/10.1002/9780470549148

Xing Y, Wang M, Wang J, Nie Z, Wu G, Yang X, Shen Y. 2019. Dimerization of MICU proteins controls Ca^{2+}Influx through the mitochondrial Ca^{2+} uniporter. *Cell Reports* **26**:1203–1212. DOI: https://doi.org/10.1016/j.celrep.2019.01.022, PMID: 30699349

Yoo J, Wu M, Yin Y, Herzik MA, Lander GC, Lee SY. 2018. Cryo-EM structure of a mitochondrial calcium uniporter. *Science* **361**:506–511. DOI: https://doi.org/10.1126/science.aar4056, PMID: 29954988

Zhuo W, Zhou H, Guo R, Yi J, Zhang L, Yu L, Sui Y, Zeng W, Wang P, Yang M. 2021. Structure of intact human MCU supercomplex with the auxiliary MICU subunits. *Protein & Cell* **12**:220–229. DOI: https://doi.org/10.1007/s13238-020-00776-w, PMID: 32862359